fractal and fractional

MDPI

Article

Hierarchies of Arnold Tongues Generated by High-Dimensional Nilpotent Matrices

Rasa Smidtaite, Ugne Orinaite and Minvydas Ragulskis *

Research Group for Nonlinear Systems, Kaunas University of Technology, Studentu 50-146, LT-51368 Kaunas, Lithuania; rasa.smidtaite@ktu.lt (R.S.); ugne.orinaite@ktu.lt (U.O.)
* Correspondence: minvydas.ragulskis@ktu.lt; Tel.: +370-698-22456

Abstract

Arnold tongues are wedge-shaped regions in parameter space associated with mode locking and synchronization phenomena in nonlinear dynamical systems. The Caputo fractional standard map extends the classical standard map by incorporating long-memory effects through fractional derivatives and is known to generate Arnold tongue structures as the fractionality parameter approaches unity. In this paper, we investigate the fractional standard map applied to matrix-valued state variables, with particular emphasis on systems governed by high-dimensional nilpotent matrices. We show that the interplay between fractional memory and nilpotent algebra produces hierarchical families of Arnold tongues associated with divergent dynamics. This phenomenon is not observed in either the classical standard map or the non-fractional standard map of nilpotent matrices alone. For idempotent matrices, the fractional standard map retains the same level of dynamical complexity as its scalar counterpart. For nilpotent matrices, higher-order terms induce coupling between the map coefficients, giving rise to substantially richer dynamical behavior. This combination of fractional memory and nilpotent algebra provides a systematic framework for studying higher-dimensional nonlinear dynamics beyond the scalar setting. To support numerical investigations, an efficient computational scheme for the auxiliary parameters is derived and calibrated using the H-rank algorithm, which provides a concise measure of algebraic complexity in sequences generated by dynamical systems. Numerical simulations reveal hierarchical structures of Arnold tongues of divergence together with characteristic divergence rates of the auxiliary parameters. The hierarchical level of a given auxiliary parameter is identified as a key quantity determining the algebraic complexity of the transient dynamics, with potential implications for information encoding in applications exploiting transient dynamical processes.

Keywords: Arnold tongue; fractional maps; divergence rate

Academic Editor: António Lopes

Received: 27 April 2026
Revised: 8 June 2026
Accepted: 9 June 2026
Published: 11 June 2026

1. Introduction

Arnold tongues are wedge-shaped regions in parameter space associated with mode locking, where a nonlinear periodically forced system synchronizes with the external forcing so that the frequency ratio becomes a rational number, resulting in phase-locked periodic dynamics [1–3]. Arnold tongues are commonly observed in systems such as the circle map [4–6], forced oscillators [7–9], Josephson junctions [10–13], electronic circuits [14–16], lasers [17–19], and biological rhythms [20–23]. They are widely used in the study of synchronization phenomena [24–26], nonlinear resonance [27,28], and frequency locking in physics [29–31], engineering [32,33], and biological systems [34–36].

Among the dynamical systems used to study resonance and chaotic behavior, the standard map (Chirikov–Taylor map) plays a fundamental role in nonlinear dynamics [37,38] and transport processes in conservative systems [39,40]. The standard map is an area-preserving map widely used to investigate Hamiltonian chaos [38,41]. Although Arnold tongues do not appear directly in the standard map, it is closely related to the circle map, where such structures arise. Therefore, the standard map contributes to understanding the dynamical mechanisms underlying synchronization and frequency-locking phenomena. The relevance between the standard and circle maps becomes particularly apparent when fractional generalizations are introduced, such as formulations based on Caputo [42–44] or Liouville [45] fractional derivatives, or fractional differences [46,47]. In these cases, as the fractional order approaches one, the fractional standard map approaches the classical circle map [48], allowing the emergence and investigation of Arnold tongue structures [49].

The Caputo fractional derivative is particularly well suited for discrete dynamical systems because it preserves the standard form of initial conditions and admits a clear physical interpretation in terms of power-law memory. Unlike the Riemann–Liouville derivative, the Caputo derivative of a constant vanishes, which ensures consistency with classical initial value problems. In the context of iterative maps, the Caputo formulation introduces a convolution-type memory kernel that weights all past states with algebraically decaying coefficients so that the entire history of the trajectory contributes to each update. This long-memory mechanism is responsible for the slow power-law decay of correlations, the suppression of chaotic diffusion, and the emergence of Arnold tongue structures in the fractional standard map as the fractional order α approaches unity [42,49]. These properties make the Caputo fractional standard map a natural and well-motivated framework for investigating the interplay between memory effects and nonlinear dynamics.

The Caputo fractional standard map exhibits a rich variety of dynamical behaviors that depend sensitively on the fractional order α and the nonlinearity parameter K. As α varies between 1 and 2, the system undergoes a complex transition from the circle map, where Arnold tongue structures and mode-locking dominate, to the classical standard map, where Hamiltonian chaos and large-scale diffusion prevail. In the intermediate fractional regime, the power-law memory kernel introduces long transients and suppresses chaotic diffusion, producing an intricate interplay between regular, quasiperiodic, and chaotic dynamics [42,49]. This sensitivity to the fractional order makes the Caputo fractional standard map a particularly rich dynamical system for investigating the role of memory in nonlinear phenomena.

While one possible direction for extending classical discrete maps is fractionalization [42,45,48,49], another approach is replacing the scalar map variable with a matrix of variables [50], allowing the system to capture higher-dimensional interactions. The introduction of matrix variables has been shown to produce new dynamical effects, including finite-time divergence and explosive instability [51,52], and has suggested applications in image hiding [53,54], synchronization [55], and pattern formation [54]. It also has revealed novel phenomena, such as diverging spiral waves in the Barkley model [56] and diverging phase dynamics in the Chialvo hyperneuron model [57].

Since the classical standard map serves as a paradigmatic area-preserving chaotic map, it provides a natural starting point for several important generalizations. Two natural extensions arise from incorporating fractional memory and from introducing matrix-valued dynamics. The fractional standard map incorporates long-memory effects through fractional derivatives [43,49,58]. In contrast, the nilpotent version of the standard map replaces the scalar state variable by matrices with the nilpotent structure, leading to fundamentally different behavior characterized by diverging transient processes and the absence of Arnold tongues [52]. The Caputo standard map of matrices studied in this work combines

these two extensions. The interaction between fractional dynamics and nilpotent algebra produces a new dynamical regime in which Arnold tongues reappear in the form of hierarchical structures of divergence, a phenomenon not observed in either the classical standard map or the standard map of nilpotent matrices alone.

The proposed framework builds on a series of prior works by our research group. The theoretical foundation for nilpotent matrix dynamics in iterative maps was established in [52], where the conditions for exponential divergence were derived. The Caputo fractional standard map in the scalar setting was investigated in [49], where Arnold tongue structures were identified. The most direct predecessor of the current manuscript is [59], where Arnold tongues of divergence were studied in the Caputo fractional standard map of nilpotent matrices, but limited to the 2×2 matrix case.

The current manuscript makes the following original contributions that go beyond all prior works: First, the framework is extended from 2×2 to high-dimensional nilpotent matrices of order n, which is not straightforward since higher-order nilpotent terms induce coupling between the map coefficients that does not appear in the 2×2 case. Second, this coupling gives rise to hierarchical families of Arnold tongues of divergence, a phenomenon not observed in the 2×2 setting or the central finding of the paper. Third, an efficient computational scheme for the auxiliary parameters is derived, replacing falling factorial expressions with iteratively computed coefficients. Fourth, the hierarchical level of a given auxiliary parameter is identified as a key quantity determining the algebraic complexity of the transient dynamics.

This article has two main goals. The first is to develop a rigorous formulation of the Caputo fractional standard map for matrix-valued states, with special emphasis on nilpotent matrices and the resulting hierarchical dynamics. The second is to analyze the dynamical structures emerging in these systems, including divergence boundaries, hierarchical Arnold tongues, and characteristic divergence rates, and to demonstrate how the H-rank algorithm [60] can be used to measure the algebraic complexity of the generated sequences.

This manuscript is structured as follows: Section 2 presents the preliminaries, including the fractional standard map and the definitions of idempotent and nilpotent matrices. Section 3 introduces the fractional standard map for matrices, with separate formulations for idempotent and nilpotent matrices and the corresponding computational scheme. Section 4 describes the calibration of the numerical scheme and the H-rank algorithm used for parameter estimation. Section 5 presents computational simulations, including the hierarchies of Arnold tongues and the scaling behavior of the auxiliary parameters. Discussion and concluding remarks are given in the final section.

2. Preliminaries

2.1. The Fractional Standard Map

The Caputo fractional standard map is given by [48,49]:

$$\begin{aligned} p^{(t+1)} &= p^{(t)} - \tfrac{K}{\Gamma(\alpha-1)} \left(\sum_{r=0}^{t-1} V_\alpha^2(t-r+1) \sin x^{(r)} + \sin x^{(t)} \right), \quad (\mathrm{mod}\, 2\pi), \\ x^{(t+1)} &= x^{(t)} + p^{(0)} - \tfrac{K}{\Gamma(\alpha)} \sum_{r=0}^{t} V_\alpha^1(t-r+1) \sin x^{(r)}, \quad (\mathrm{mod}\, 2\pi), \end{aligned} \tag{1}$$

where $t = 0, 1, \ldots$; K denotes the forcing amplitude; α is the fractional order ($1 < \alpha \leq 2$); and V_α^s is given by:

$$V_\alpha^s(m) = m^{\alpha-s} - (m-1)^{\alpha-s}, \quad m = 1, 2, \ldots, \tag{2}$$

where $s \in \{1, 2\}$ corresponds to the kernels appearing in the second and first sums of Equation (1), respectively.

At the initial iteration $t = 0$, the summation $\sum_{r=0}^{t-1} V_\alpha^2(t - r + 1) \sin x^{(r)}$ in Equation (1) is omitted. Consequently, $p^{(1)} = p^{(0)} - \frac{K}{\Gamma(\alpha-1)} \sin x^{(0)}$, where the resulting value is taken modulo 2π and $x^{(0)}$ is set to 0 [48]. The fractional standard map is a special case of a fractional generalized map [61]. The fractional standard map reduces to the non-fractional standard map at $\alpha = 2$ but is not automatically reduced to the circle map at $\alpha = 1$ [62]. However, a clear pattern of Arnold tongues emerges when the fractionality parameter α tends to 1 [59]. Therefore, the fractional standard map can be considered to be the fractional counterpart of the paradigmatic circle map [59].

2.2. Idempotents and Nilpotents of Order n

Before discussing fractional matrix maps in detail, we introduce special forms of $n \times n$ matrices.

Let us construct a square matrix $\mathbf{X}$ with all distinct eigenvalues $\rho_1 \neq \rho_2 \neq \cdots \neq \rho_n$; $\rho_j \in \mathbb{R}$ $(j = 1, 2, \ldots, n)$. A matrix of this type can be represented as an idempotent matrix [52]:

$$\mathbf{X} = \rho_1 \mathbf{D}_1 + \rho_2 \mathbf{D}_2 + \cdots + \rho_n \mathbf{D}_n, \tag{3}$$

where $\mathbf{D}_j$ $(j = 1, \ldots, n)$ are mutually commuting orthogonal conjugate idempotents satisfying $\sum_{j=1}^{n} \mathbf{D}_j = \mathbf{I}$ ($\mathbf{I}$ denotes the identity matrix). Each matrix $\mathbf{D}_j$ is similar to a diagonal matrix with a single nonzero element $d_{j,j}$ and all remaining entries equal to zero:

$$\mathbf{D}_j = \mathbf{T} \begin{bmatrix} 0 & \ldots & 0 & \ldots & 0 \\ \vdots & \ddots & \vdots & \ddots & \vdots \\ 0 & \ldots & d_{j,j} & \ldots & 0 \\ \vdots & \ddots & \vdots & \ddots & \vdots \\ 0 & \ldots & 0 & \ldots & 0 \end{bmatrix} \mathbf{T}^{-1}, \quad \mathbf{T} \in \mathbb{R}^{n \times n}, \quad \det \mathbf{T} \neq 0. \tag{4}$$

Matrices $\mathbf{D}_j$ satisfy

$$\det \mathbf{D}_j = 0, \quad \mathbf{D}_i \cdot \mathbf{D}_j = \begin{cases} \mathbf{D}_i, & \text{if } i = j, \\ \mathbf{\Theta}, & \text{if } i \neq j, \quad i, j = 1, 2, \ldots, n, \end{cases} \tag{5}$$

where $\mathbf{\Theta}$ denotes the zero matrix.

Now, let us proceed with a matrix that exhibits the opposite structural properties. Let us construct a square matrix $\mathbf{X}$ with all equal eigenvalues $\rho_1 = \rho_2 = \cdots = \rho_n = \rho_0$ ($\rho_0 \in \mathbb{R}$). Then this matrix can be represented as a nilpotent matrix [52]:

$$\mathbf{X} = \rho_j \mathbf{I} + \mu_1 \mathbf{N}_1 + \mu_2 \mathbf{N}_2 + \cdots + \mu_{n-1} \mathbf{N}_{n-1}, \tag{6}$$

where $\mu_j \in \mathbb{R}$ $(j = 1, 2, \ldots, n - 1)$ and nilpotents $\mathbf{N}_j$ are constructed via similarity transformation from an inner matrix with ones on the jth super-diagonal and all other zeros entries:

$$\mathbf{N}_j = \mathbf{T} \begin{bmatrix} 0 & \ldots & n_{1,j+1} & 0 & \ldots & 0 \\ 0 & \ldots & 0 & n_{2,j+1} & \ldots & 0 \\ \vdots & \ddots & \vdots & \vdots & \ldots & \vdots \\ 0 & \ldots & 0 & 0 & \ldots & 0 \end{bmatrix} \mathbf{T}^{-1}, \quad \mathbf{T} \in \mathbb{R}^{n \times n}, \quad \det \mathbf{T} \neq 0. \tag{7}$$

The determinants of nilpotent $\mathbf{N}_j$ $(j = 1, 2, \ldots, n - 1)$ are each equal to zero $\det \mathbf{N}_j = 0$. Although each nilpotent matrix is singular, their products reveal structural patterns fundamental to matrix decomposition. The products of nilpotents are depicted in Table 1.

Table 1. The multiplicity of nth-order nilpotents $\mathbf{N}_j, j = 1, 2, \ldots, n-1$.

·	$\mathbf{N}_1$	$\mathbf{N}_2$	$\mathbf{N}_3$	$\mathbf{N}_4$	…	$\mathbf{N}_{n-2}$	$\mathbf{N}_{n-1}$
$\mathbf{N}_1$	$\mathbf{N}_2$	$\mathbf{N}_3$	$\mathbf{N}_4$	$\mathbf{N}_5$	…	$\mathbf{N}_{n-1}$	$\boldsymbol{\Theta}$
$\mathbf{N}_2$	$\mathbf{N}_3$	$\mathbf{N}_4$	$\mathbf{N}_5$	$\mathbf{N}_6$	…	$\boldsymbol{\Theta}$	$\boldsymbol{\Theta}$
$\mathbf{N}_3$	$\mathbf{N}_4$	$\mathbf{N}_5$	$\mathbf{N}_6$	$\mathbf{N}_7$	…	$\boldsymbol{\Theta}$	$\boldsymbol{\Theta}$
$\mathbf{N}_4$	$\mathbf{N}_5$	$\mathbf{N}_6$	$\mathbf{N}_7$	$\mathbf{N}_8$	…	$\boldsymbol{\Theta}$	$\boldsymbol{\Theta}$
⋮	⋮	⋮	⋮	⋮	⋱	⋮	⋮
$\mathbf{N}_{n-2}$	$\mathbf{N}_{n-1}$	$\boldsymbol{\Theta}$	$\boldsymbol{\Theta}$	$\boldsymbol{\Theta}$	…	$\mathbf{N}_{n-1}$	$\boldsymbol{\Theta}$
$\mathbf{N}_{n-1}$	$\boldsymbol{\Theta}$	$\boldsymbol{\Theta}$	$\boldsymbol{\Theta}$	$\boldsymbol{\Theta}$	…	$\boldsymbol{\Theta}$	$\boldsymbol{\Theta}$

Note that nilpotents $\mathbf{N}_i$ and $\mathbf{N}_j$ obey the following commutative rule:

$$\mathbf{N}_i \cdot \mathbf{N}_j = \mathbf{N}_j \cdot \mathbf{N}_i = \begin{cases} \mathbf{N}_{i+j}, & \text{if } i+j \le n-1; \\ \boldsymbol{\Theta}, & \text{if } i+j \ge n, \quad i,j = 1,2,\ldots,n, \end{cases} \tag{8}$$

which directly leads to:

$$\left(\mathbf{N}_j\right)^{j+1} = \boldsymbol{\Theta}. \tag{9}$$

Note that a square matrix of order n may exhibit various eigenvalue configurations and, consequently, admit forms other than the idempotent form (3) or the nilpotent form (6). For example, it may possess 3 distinct eigenvalues and $n-3$ repeated eigenvalues. The packing codes introduced in [52] provide a framework for characterizing the structural types of $n \times n$ matrices and for analyzing their divergence rates in nonlinear matrix maps. The simplest case occurs for $n = 2$, where only two scenarios are possible: the eigenvalues coincide or are distinct. These cases, described in [50,51], have been thoroughly investigated in various models [55,56,63].

3. A Matrix Formulation of the Fractional Standard Map for $n \times n$ Matrices

The scalar iterates $x^{(t)}$ and $p^{(t)}$ in Equation (1) may be generalized to an $n \times n$ matrix-valued variable $\mathbf{X}^{(t)} = \begin{bmatrix} x_{11}^{(t)} & \cdots & x_{1n}^{(t)} \\ \vdots & \ddots & \vdots \\ x_{n1}^{(t)} & \cdots & x_{nn}^{(t)} \end{bmatrix}$ with $x_{11}^{(t)}, x_{12}^{(t)}, \ldots, x_{nn}^{(t)} \in \mathbb{R}$, and $\mathbf{P}^{(t)} = \begin{bmatrix} p_{11}^{(t)} & \cdots & p_{1n}^{(t)} \\ \vdots & \ddots & \vdots \\ p_{n1}^{(t)} & \cdots & p_{nn}^{(t)} \end{bmatrix}$ with $p_{11}^{(t)}, p_{12}^{(t)}, \ldots, p_{nn}^{(t)} \in \mathbb{R}$.

Then, the fractional map takes the following form [59]:

$$\begin{aligned} \mathbf{P}^{(t+1)} &= \mathbf{P}^{(t)} - \tfrac{K}{\Gamma(\alpha-1)} \left(\sum_{r=0}^{t-1} V_\alpha^2(t-r+1) \sin \mathbf{X}^{(r)} + \sin \mathbf{X}^{(t)} \right), \quad (\mathrm{mod}\, 2\pi), \\ \mathbf{X}^{(t+1)} &= \mathbf{X}^{(t)} + \mathbf{P}^{(0)} - \tfrac{K}{\Gamma(\alpha)} \sum_{r=0}^{t} V_\alpha^1(t-r+1) \sin \mathbf{X}^{(r)}, \quad (\mathrm{mod}\, 2\pi), \end{aligned} \tag{10}$$

where $t = 0, 1, \ldots$; the modulo reduction $(\mathrm{mod}\, 2\pi)$ is applied spectrally to the updated matrices $\mathbf{P}^{(t+1)}$ and $\mathbf{X}^{(t+1)}$, with their eigenvalues reduced modulo 2π; and the matrix sine function $\sin(\mathbf{X})$ is defined through its convergent power series

$$\sin(\mathbf{X}) = \sum_{j=0}^{\infty} \frac{(-1)^j}{(2j+1)!} \mathbf{X}^{2j+1}. \tag{11}$$

3.1. A Matrix Formulation of the Fractional Standard Map for $n \times n$ Idempotent Matrices

We first examine the case where the matrices involved are idempotent. The guiding principle is that if a matrix decomposes into a sum of orthogonal idempotents, then analytic

functions act on each component independently. This mirrors the scalar spectral theorem but relies on algebraic idempotents rather than orthogonal projectors.

Corollary 1. *Let $\mathbf{P} \in \mathbb{R}^{n\times n}$ be of the form $\mathbf{P} = \sum_{j=1}^{n} c_j \mathbf{D}_j$, where $\{\mathbf{D}_j\}_{j=1}^{n}$ is a family of mutually orthogonal conjugate idempotents and $c_1, \ldots, c_n \in \mathbb{R}$. Then, for every analytic function f, one has*

$$f(\mathbf{P}) = \sum_{j=1}^{n} f(c_j)\, \mathbf{D}_j. \tag{12}$$

Proof. Let f be an analytic function admitting a Taylor expansion about a point c:

$$f(z) = \sum_{m=0}^{\infty} \frac{f^{(m)}(c)}{m!}(z-c)^m. \tag{13}$$

Applying this expansion to a matrix yields:

$$f(\mathbf{P}) = \sum_{m=0}^{\infty} \frac{f^{(m)}(c)}{m!}(\mathbf{P}-c\mathbf{I})^m. \tag{14}$$

Since f is analytic on a neighborhood containing the spectrum $\sigma(\mathbf{P}) = \{c_1, \ldots, c_n\}$, the above matrix series converges absolutely in any submultiplicative matrix norm and therefore defines $f(\mathbf{P})$.

Now substitute the decomposition $\mathbf{P} = \sum_{j=1}^{n} c_j \mathbf{D}_j$, recalling that $\sum_{j=1}^{n} \mathbf{D}_j = \mathbf{I}$. Then

$$\mathbf{P} - c\mathbf{I} = \sum_{j=1}^{n} (c_j - c)\mathbf{D}_j. \tag{15}$$

Using the relations $\mathbf{D}_i\mathbf{D}_j = \mathbf{\Theta}$ for $i \neq j$ (and hence $\mathbf{D}_i\mathbf{D}_j = \mathbf{D}_j\mathbf{D}_i$) together with $\mathbf{D}_j^2 = \mathbf{D}_j$, it follows by induction on m that

$$(\mathbf{P} - c\mathbf{I})^m = \sum_{j=1}^{n} (c_j - c)^m \mathbf{D}_j, \qquad m \geq 0. \tag{16}$$

The statement is immediate for $m = 1$. Assume that it holds for some $m \geq 1$. Then

$$\begin{aligned}(\mathbf{P} - c\mathbf{I})^{m+1} &= \left(\sum_{j=1}^{n} (c_j - c)^m \mathbf{D}_j\right)\left(\sum_{k=1}^{n} (c_k - c)\mathbf{D}_k\right) \\ &= \sum_{j=1}^{n}\sum_{k=1}^{n} (c_j - c)^m (c_k - c)\mathbf{D}_j\mathbf{D}_k.\end{aligned} \tag{17}$$

Since $\mathbf{D}_j\mathbf{D}_k = \mathbf{\Theta}$ whenever $j \neq k$ and $\mathbf{D}_j^2 = \mathbf{D}_j$, all mixed terms vanish and therefore

$$(\mathbf{P} - c\mathbf{I})^{m+1} = \sum_{j=1}^{n} (c_j - c)^{m+1} \mathbf{D}_j. \tag{18}$$

Hence, (16) holds for all $m \geq 0$. Consequently,

$$f(\mathbf{P}) = \sum_{m=0}^{\infty} \frac{f^{(m)}(c)}{m!}(\mathbf{P} - c\mathbf{I})^m = \sum_{m=0}^{\infty} \frac{f^{(m)}(c)}{m!}\left(\sum_{j=1}^{n} (c_j - c)^m \mathbf{D}_j\right). \tag{19}$$

Since the sum over j is finite, the order of summation may be interchanged:

$$f(\mathbf{P}) = \sum_{m=0}^{\infty} \frac{f^{(m)}(c)}{m!} \left(\sum_{j=1}^{n} (c_j - c)^m \mathbf{D}_j \right) = \sum_{j=1}^{n} \left(\sum_{m=0}^{\infty} \frac{f^{(m)}(c)}{m!} (c_j - c)^m \right) \mathbf{D}_j, \tag{20}$$

because for each j, the inner series is precisely the Taylor expansion of f evaluated at c_j. Thus,

$$f(\mathbf{P}) = \sum_{j=1}^{n} f(c_j) \mathbf{D}_j. \tag{21}$$

□

Each idempotent component evolves independently: f acts directly on the scalar coefficients c_j, while the family of idempotents $\{\mathbf{D}_j\}_{j=1}^{n}$ remains unchanged.

Lemma 1. *Let the initial matrices be idempotent sharing a decomposition in a common family of conjugate idempotents:*

$$\mathbf{P}^{(0)} = \sum_{j=1}^{n} \rho_{j,p}^{(0)} \mathbf{D}_j, \quad \mathbf{X}^{(0)} = \sum_{j=1}^{n} \rho_{j,x}^{(0)} \mathbf{D}_j. \tag{22}$$

Assume that scalars $\rho_{j,p}^{(0)} \neq \rho_{l,p}^{(0)}$ and $\rho_{j,x}^{(0)} \neq \rho_{l,x}^{(0)}$ if $j \neq l$; $\rho_{j,p}^{(0)}, \rho_{j,x}^{(0)} \in \mathbb{R}$. Then, for $t = 0, 1, \ldots$, the matrices $\mathbf{P}^{(t+1)}$ and $\mathbf{X}^{(t+1)}$ defined by (10) remain idempotent and admit decompositions with the same family of conjugate idempotents $\{\mathbf{D}j\}$. Moreover, their iterations can be written component-wise as

$$\mathbf{P}^{(t+1)} = \sum_{j=1}^{n} \rho_{j,p}^{(t+1)} \mathbf{D}_j, \quad \mathbf{X}^{(t+1)} = \sum_{j=1}^{n} \rho_{j,x}^{(t+1)} \mathbf{D}_j \tag{23}$$

where

$$\begin{aligned} \rho_{j,p}^{(t+1)} &= \rho_{j,p}^{(t)} - \frac{K}{\Gamma(\alpha-1)} \left[\sum_{r=0}^{t-1} V_{\alpha}^{2}(t-r+1) \sin\left(\rho_{j,x}^{(r)}\right) + \sin\left(\rho_{j,x}^{(t)}\right) \right], \quad (\mathrm{mod}\, 2\pi), \\ \rho_{j,x}^{(t+1)} &= \rho_{j,x}^{(t)} + \rho_{j,p}^{(0)} - \frac{K}{\Gamma(\alpha)} \left[\sum_{r=0}^{t} V_{\alpha}^{1}(t-r+1) \sin\left(\rho_{j,x}^{(r)}\right) \right], \quad (\mathrm{mod}\, 2\pi), \end{aligned} \tag{24}$$

for $j = 1, 2, \ldots, n$.

Proof. The map of matrices $\mathbf{P}^{(t)}$ and $\mathbf{X}^{(t)}$ yields:

$$\begin{aligned} \mathbf{P}^{(t+1)} = &\left(\sum_{j=1}^{n} \rho_{j,p}^{(t)} \mathbf{D}_j \right) \\ &- \frac{K}{\Gamma(\alpha-1)} \left[\sum_{r=0}^{t-1} V_{\alpha}^{2}(t-r+1) \sin\left(\sum_{j=1}^{n} \rho_{j,x}^{(r)} \mathbf{D}_j \right) + \sin\left(\sum_{j=1}^{n} \rho_{j,x}^{(t)} \mathbf{D}_j \right) \right]. \end{aligned} \tag{25}$$

According to Corollary 1, Equation (25) takes the following form:

$$\begin{aligned} \mathbf{P}^{(t+1)} = &\left(\sum_{j=1}^{n} \rho_{j,p}^{(t)} \mathbf{D}_j \right) \\ &- \frac{K}{\Gamma(\alpha-1)} \left[\sum_{r=0}^{t-1} V_{\alpha}^{2}(t-r+1) \left(\sum_{j=1}^{n} \sin\left(\rho_{j,x}^{(r)}\right) \mathbf{D}_j \right) + \left(\sum_{j=1}^{n} \sin\left(\rho_{j,x}^{(t)}\right) \mathbf{D}_j \right) \right]. \end{aligned} \tag{26}$$

The rearrangement of sums in Equation (26) gives the expression of the idempotent matrix $\mathbf{P}^{(t+1)}$:

$$\mathbf{P}^{(t+1)} = \sum_{j=1}^{n} \rho_{j,p}^{(t+1)} \mathbf{D}_j, \tag{27}$$

where

$$\rho_{j,p}^{(t+1)} = \rho_{j,p}^{(t)} - \frac{K}{\Gamma(\alpha-1)} \left[\sum_{r=0}^{t-1} V_\alpha^2(t-r+1) \sin\left(\rho_{j,x}^{(r)}\right) + \sin\left(\rho_{j,x}^{(t)}\right) \right], \quad (\mathrm{mod}\, 2\pi). \tag{28}$$

The expression of $\mathbf{X}^{(t+1)}$ in (10) is derived analogously by substituting the idempotent decompositions $\mathbf{X}^{(t)} = \sum_{j=1}^{n} \rho_{j,x}^{(t)} \mathbf{D}_j$ and $\mathbf{P}^{(0)} = \sum_{j=1}^{n} \rho_{j,p}^{(0)} \mathbf{D}_j$, expanding $\sin\left(\mathbf{X}^{(r)}\right)$ according to Corollary 1, and rearranging the sums:

$$\begin{aligned} \mathbf{X}^{(t+1)} &= \left(\sum_{j=1}^{n} \rho_{j,x}^{(t)} \mathbf{D}_j \right) + \left(\sum_{j=1}^{n} \rho_{j,p}^{(0)} \mathbf{D}_j \right) - \frac{K}{\Gamma(\alpha)} \sum_{r=0}^{t} V_\alpha^1(t-r+1) \sin\left(\sum_{j=1}^{n} \rho_{j,x}^{(r)} \mathbf{D}_j \right) \\ &= \left(\sum_{j=1}^{n} \rho_{j,x}^{(t)} \mathbf{D}_j \right) + \left(\sum_{j=1}^{n} \rho_{j,p}^{(0)} \mathbf{D}_j \right) - \frac{K}{\Gamma(\alpha)} \sum_{r=0}^{t} V_\alpha^1(t-r+1) \left(\sum_{j=1}^{n} \sin\left(\rho_{j,x}^{(r)}\right) \mathbf{D}_j \right) \\ &= \sum_{j=1}^{n} \left(\rho_{j,x}^{(t)} + \rho_{j,p}^{(0)} - \frac{K}{\Gamma(\alpha)} \sum_{r=0}^{t} V_\alpha^1(t-r+1) \sin\left(\rho_{j,x}^{(r)}\right) \right) \mathbf{D}_j. \end{aligned} \tag{29}$$

Therefore, $\mathbf{X}^{(t+1)}$ is also an idempotent matrix:

$$\mathbf{X}^{(t+1)} = \sum_{j=1}^{n} \rho_{j,x}^{(t+1)} \mathbf{D}_j, \tag{30}$$

where

$$\rho_{j,x}^{(t+1)} = \rho_{j,x}^{(t)} + \rho_{j,p}^{(0)} - \frac{K}{\Gamma(\alpha)} \sum_{r=0}^{t} V_\alpha^1(t-r+1) \sin\left(\rho_{j,x}^{(r)}\right), \quad (\mathrm{mod}\, 2\pi). \tag{31}$$

□

Lemma 1 establishes that the idempotent fractional standard map reduces to $2n$ scalar maps of eigenvalues, yielding n uncoupled fractional standard maps:

$$\begin{cases} \rho_{j,p}^{(t+1)} = \rho_{j,p}^{(t)} - \frac{K}{\Gamma(\alpha-1)} \left(\sum_{r=0}^{t-1} V_\alpha^2(t-r+1) \sin \rho_{j,x}^{(r)} + \sin \rho_{j,x}^{(t)} \right), \quad (\mathrm{mod}\, 2\pi), \\ \rho_{j,x}^{(t+1)} = \rho_{j,x}^{(t)} + \rho_{j,p}^{(0)} - \frac{K}{\Gamma(\alpha)} \sum_{r=0}^{t} V_\alpha^1(t-r+1) \sin \rho_{j,x}^{(r)}, \quad (\mathrm{mod}\, 2\pi), \quad t = 0, 1, \ldots, \end{cases} \tag{32}$$

where $j = 1, 2, \ldots, n$.

In other words, the fractional idempotent standard map exhibits a level of complexity comparable to its scalar counterpart.

3.2. A Matrix Formulation of the Fractional Standard Map for $n \times n$ Nilpotent Matrices

In contrast to idempotents, nilpotents do not admit diagonalization. Instead, nilpotents interact through algebraic multiplication. Analytic functions of such matrices can be treated via Taylor expansions, while products of nilpotents combine into higher-order nilpotents that eventually vanish.

Corollary 2. *Let* $\mathbf{P} \in \mathbb{R}^{n\times n}$ *be defined as:*

$$\mathbf{P} = c_0\mathbf{I} + \sum_{j=1}^{n-1} c_j\mathbf{N}_j, \tag{33}$$

where $c_0, c_j \in \mathbb{R}$, $c_1 \neq 0$; *each* $\mathbf{N}_j$ $(j = 1, 2, \ldots, n-1)$ *is a matrix nilpotent with a nilpotency index equal to* $j+1$ *and* $\mathbf{N}_j \cdot \mathbf{N}_l = \mathbf{N}_{j+l}$ *if* $j + l \leq n-1$, *and* $\mathbf{\Theta}$ *otherwise* $(j, l = 1, 2, \ldots, n-1)$. *If* f *is an analytic function, then*

$$f(\mathbf{P}) = f(c_0)\mathbf{I} + \sum_{j=1}^{n-1}\left(\sum_{m=1}^{j}\frac{f^{(m)}(c_0)}{m!}\sum_{\substack{i_1+i_2+\cdots+i_m=j\\ i_1,i_2,\ldots,i_m\geq 1}} c_{i_1}c_{i_2}\cdots c_{i_m}\right)\mathbf{N}_j, \tag{34}$$

where $f^{(m)}(c_0)$ *denotes the m-th derivative of the function* f *evaluated at* c_0.

Proof. Let f be an analytic function that can be expanded into a Taylor series:

$$f(z) = \sum_{m=0}^{\infty}\frac{f^{(m)}(c_0)}{m!}(z - c_0)^m. \tag{35}$$

Since f is analytic on a neighborhood containing the spectrum of $\mathbf{P}$, and $\sigma(\mathbf{P}) = \{c_0\}$ because $\mathbf{P} = c_0\mathbf{I} + \sum_{j=1}^{n-1} c_j\mathbf{N}_j$ differs from $c_0\mathbf{I}$ by a nilpotent matrix, the matrix Taylor series defining $f(\mathbf{P})$ converges absolutely in any submultiplicative matrix norm. Let

$$\mathbf{Q} = \mathbf{P} - c_0\mathbf{I} = \sum_{j=1}^{n-1} c_j\mathbf{N}_j. \tag{36}$$

Since $\mathbf{N}_j\mathbf{N}_l = \mathbf{N}_{j+l}$ when $j + l \leq n-1$ and $\mathbf{N}_j\mathbf{N}_l = \mathbf{\Theta}$ otherwise, every term arising in the expansion of $\mathbf{Q}^m$ has the form

$$c_{i_1}c_{i_2}\cdots c_{i_m}\mathbf{N}_{i_1+i_2+\cdots+i_m}, \tag{37}$$

where $i_1, \ldots, i_m \geq 1$. Since

$$i_1 + i_2 + \cdots + i_m \geq m, \tag{38}$$

it follows that for $m \geq n$, one has $i_1 + \cdots + i_m \geq n$, and therefore every such product is equal to $\mathbf{\Theta}$. Consequently,

$$\mathbf{Q}^m = \mathbf{\Theta}, \qquad m \geq n. \tag{39}$$

Hence, $\mathbf{Q}$ is nilpotent of index at most n. Therefore,

$$f(\mathbf{P}) = \sum_{m=0}^{\infty}\frac{f^{(m)}(c_0)}{m!}(\mathbf{P} - c_0\mathbf{I})^m = \sum_{m=0}^{n-1}\frac{f^{(m)}(c_0)}{m!}(\mathbf{P} - c_0\mathbf{I})^m, \tag{40}$$

since $(\mathbf{P} - c_0\mathbf{I})^m = \mathbf{\Theta}$ for all $m \geq n$. Hence,

$$f(\mathbf{P}) = f(c_0)\mathbf{I} + \sum_{m=1}^{n-1}\frac{f^{(m)}(c_0)}{m!}\left(\sum_{j=1}^{n-1} c_j\mathbf{N}_j\right)^m. \tag{41}$$

Applying the multinomial formula [64] and using the multiplication rule $\mathbf{N}_j\mathbf{N}_l = \mathbf{N}_{j+l}$, we obtain

$$f(\mathbf{P}) = f(c_0)\mathbf{I} + \sum_{j=1}^{n-1}\left(\sum_{m=1}^{j}\frac{f^{(m)}(c_0)}{m!}\sum_{\substack{i_1+i_2+\cdots+i_m=j\\ i_1,i_2,\ldots,i_m\geq 1}} c_{i_1}c_{i_2}\cdots c_{i_m}\right)\mathbf{N}_j. \tag{42}$$

The interchange between the finite sum over m and the collection of coefficients of $\mathbf{N}_j$ is legitimate because the Taylor series has already reduced to the finite polynomial above. □

Note that the upper limit of the inner summation is j rather than $n-1$. This is because each index $i_k \geq 1$, so the condition $i_1 + i_2 + \cdots + i_m = j$ with m positive integers requires $m \leq j$. For $m > j$, no partition of j into m positive integers exists, and the corresponding terms vanish. Therefore, the summation over m naturally terminates at $m = j$.

Unlike the idempotent case, cross-terms do not vanish. Instead, products of lower-order nilpotents contribute to higher-order ones, resulting in a hierarchical structure of coefficients.

In summary, Corollary 2 shows that any analytic function of a nilpotent matrix can be computed exactly via a finite Taylor series. The nilpotent multiplication rule $\mathbf{N}_j \cdot \mathbf{N}_l = \mathbf{N}_{j+l}$ couples the coefficients of different nilpotent orders, producing a hierarchical structure that is the algebraic foundation of the richer dynamical behavior observed in the fractional standard map of nilpotent matrices.

Example 1. *Consider the case where f is the sine function and the matrix order $n = 4$. Let $\mathbf{P} \in \mathbb{R}^{4\times 4}$ be defined as:*

$$\mathbf{P} = c_0\mathbf{I} + \sum_{j=1}^{3} c_j\mathbf{N}_j, \tag{43}$$

where $c_0, c_j \in \mathbb{R}$, $c_1 \neq 0$, and each $\mathbf{N}_j \in \mathbb{R}^{4\times 4}$ $(j = 1, 2, 3)$ is a nilpotent with a nilpotency index equal to $j + 1$. Then, according to (42):

$$\sin(\mathbf{P}) = \sin(c_0)\mathbf{I} + \sum_{j=1}^{3}\left(\sum_{m=1}^{j}\frac{\sin\left(c_0+\frac{m\pi}{2}\right)}{m!}\sum_{\substack{i_1+i_2+\cdots+i_m=j\\ i_1,i_2,\ldots,i_m\geq 1}} c_{i_1}c_{i_2}\cdots c_{i_m}\right)\mathbf{N}_j. \tag{44}$$

Each inner sum collects all monomials in c_j whose indices add to j.
If $j = 1$, then $m = 1$:

$$\sum_{m=1}^{1}\frac{\sin\left(c_0+\frac{1\cdot\pi}{2}\right)}{1!}\sum_{i_1=1} c_{i_1} = c_1\cos(c_0). \tag{45}$$

If $j = 2$, then $m = 1, 2$:

$$\begin{aligned}
&\sum_{m=1}^{2}\frac{\sin\left(c_0+\frac{m\pi}{2}\right)}{m!}\sum_{\substack{i_1+i_2+\cdots+i_m=j\\ i_1,i_2,\ldots,i_m\geq 1}} c_{i_1}c_{i_2}\cdots c_{i_m}\\
&\quad= \frac{\sin\left(c_0+\frac{\pi}{2}\right)}{1!}\sum_{i_1=2} c_{i_1} + \frac{\sin\left(c_0+\frac{2\cdot\pi}{2}\right)}{2!}\sum_{\substack{i_1+i_2=2\\ i_1,i_2\geq 1}} c_{i_1}c_{i_2}\\
&\quad= \frac{\sin\left(c_0+\frac{\pi}{2}\right)}{1!}c_2 + \frac{\sin\left(c_0+\frac{2\cdot\pi}{2}\right)}{2!}c_1\cdot c_1\\
&\quad= c_2\cos(c_0) - \frac{(c_1)^2\sin(c_0)}{2}.
\end{aligned} \tag{46}$$

If $j = 3$, then $m = 1, 2, 3$:

$$\begin{aligned}
&\sum_{m=1}^{3} \frac{\sin\left(c_0 + \frac{m\pi}{2}\right)}{m!} \sum_{\substack{i_1+i_2+\cdots+i_m=j \\ i_1,i_2,\ldots,i_m\geq 1}} c_{i_1} c_{i_2} \cdots c_{i_m} \\
&= \frac{\sin\left(c_0 + \frac{\pi}{2}\right)}{1!} \sum_{i_1=3} c_{i_1} + \frac{\sin\left(c_0 + \frac{2\cdot\pi}{2}\right)}{2!} \sum_{\substack{i_1+i_2=3 \\ i_1,i_2\geq 1}} c_{i_1} c_{i_2} \\
&\qquad + \frac{\sin\left(c_0 + \frac{3\cdot\pi}{2}\right)}{3!} \sum_{\substack{i_1+i_2+i_3=3 \\ i_1,i_2,i_3\geq 1}} c_{i_1} c_{i_2} c_{i_3} \\
&= \frac{\sin\left(c_0 + \frac{\pi}{2}\right)}{1!} c_3 + \frac{\sin\left(c_0 + \frac{2\cdot\pi}{2}\right)}{2!} (c_1 \cdot c_2 + c_2 \cdot c_1) + \frac{\sin\left(c_0 + \frac{3\cdot\pi}{2}\right)}{3!} c_1 \cdot c_1 \cdot c_1 \\
&= c_3 \cos(c_0) - c_1 \cdot c_2 \sin(c_0) - \frac{(c_1)^3 \cos(c_0)}{6}.
\end{aligned} \tag{47}$$

Therefore, $\sin \mathbf{P}$ *has a form of a nilpotent matrix with the same nilpotents* $\mathbf{N}_1$, $\mathbf{N}_2$, $\mathbf{N}_3$*:*

$$\begin{aligned}
\sin(\mathbf{P}) = \sin(c_0)\mathbf{I} + c_1 \cos(c_0)\mathbf{N}_1 + \left(c_2 \cos(c_0) - \frac{(c_1)^2 \sin(c_0)}{2}\right)\mathbf{N}_2 \\
+ \left(c_3 \cos(c_0) - c_1 \cdot c_2 \sin(c_0) - \frac{(c_1)^3 \cos(c_0)}{6}\right)\mathbf{N}_3.
\end{aligned} \tag{48}$$

The coefficient of each nilpotent is no longer independent: $\mathbf{N}_2$ *depends on* c_1*, and* $\mathbf{N}_3$ *depends on both* c_1 *and* c_2*. This coupling illustrates the richer algebraic structure of nilpotents.*

Lemma 2. *Let the initial matrices* $\mathbf{P}^{(0)}$ *and* $\mathbf{X}^{(0)}$ *be expressed in terms of a common family of nilpotent matrices:*

$$\mathbf{P}^{(0)} = \rho_{0,p}^{(0)}\mathbf{I} + \sum_{j=1}^{n-1} \mu_{j,p}^{(0)}\mathbf{N}_j, \quad \mathbf{X}^{(0)} = \rho_{0,x}^{(0)}\mathbf{I} + \sum_{j=1}^{n-1} \mu_{j,x}^{(0)}\mathbf{N}_j, \tag{49}$$

where $\rho_{0,p}^{(0)}, \rho_{0,x}^{(0)}, \mu_{j,p}^{(0)}, \mu_{j,x}^{(0)} \in \mathbb{R}$*; and the initial values of the auxiliary parameters* $\mu_{1,p}^{(0)}$ *and* $\mu_{1,x}^{(0)}$ *are not equal to* 0*. Then, for* $t = 0, 1, \ldots$*, the matrices* $\mathbf{P}^{(t+1)}$ *and* $\mathbf{X}^{(t+1)}$ *admit representations with the same nilpotent basis:*

$$\mathbf{P}^{(t+1)} = \rho_{0,p}^{(t+1)}\mathbf{I} + \sum_{j=1}^{n-1} \mu_{j,p}^{(t+1)}\mathbf{N}_j, \quad \mathbf{X}^{(t+1)} = \rho_{0,x}^{(t+1)}\mathbf{I} + \sum_{j=1}^{n-1} \mu_{j,x}^{(t+1)}\mathbf{N}_j, \tag{50}$$

where

$$\begin{aligned}
\rho_{0,p}^{(t+1)} &= \rho_{0,p}^{(t)} - \frac{K}{\Gamma(\alpha-1)}\left[\sum_{r=0}^{t-1} V_\alpha^2(t-r+1)\sin\left(\rho_{0,x}^{(r)}\right) + \sin\left(\rho_{0,x}^{(t)}\right)\right], \pmod{2\pi}, \\
\mu_{j,p}^{(t+1)} &= \mu_{j,p}^{(t)} \\
&\quad - \frac{K}{\Gamma(\alpha-1)}\left[\sum_{r=0}^{t-1} V_\alpha^2(t-r+1)\left(\sum_{m=1}^{j} \frac{\sin\left(\rho_{0,x}^{(r)} + \frac{m\pi}{2}\right)}{m!} \sum_{\substack{i_1+i_2+\cdots+i_m=j \\ i_1,i_2,\ldots,i_m\geq 1}} \mu_{i_1,x}^{(r)}\mu_{i_2,x}^{(r)}\cdots\mu_{i_m,x}^{(r)}\right)\right. \\
&\qquad \left. + \sum_{m=1}^{j} \frac{\sin\left(\rho_{0,x}^{(t)} + \frac{m\pi}{2}\right)}{m!} \sum_{\substack{i_1+i_2+\cdots+i_m=j \\ i_1,i_2,\ldots,i_m\geq 1}} \mu_{i_1,x}^{(t)}\mu_{i_2,x}^{(t)}\cdots\mu_{i_m,x}^{(t)}\right], \\
\rho_{0,x}^{(t+1)} &= \rho_{0,x}^{(t)} + \rho_{0,p}^{(0)} - \frac{K}{\Gamma(\alpha)}\sum_{r=0}^{t} V_\alpha^1(t-r+1)\sin\left(\rho_{0,x}^{(r)}\right), \pmod{2\pi}, \\
\mu_{j,x}^{(t+1)} &= \mu_{j,x}^{(t)} + \mu_{j,p}^{(0)} \\
&\quad - \frac{K}{\Gamma(\alpha)}\sum_{r=0}^{t} V_\alpha^1(t-r+1)\left(\sum_{m=1}^{j} \frac{\sin\left(\rho_{0,x}^{(r)} + \frac{m\pi}{2}\right)}{m!} \sum_{\substack{i_1+i_2+\cdots+i_m=j \\ i_1,i_2,\ldots,i_m\geq 1}} \mu_{i_1,x}^{(r)}\mu_{i_2,x}^{(r)}\cdots\mu_{i_m,x}^{(r)}\right),
\end{aligned} \tag{51}$$

where $t = 0, 1, \ldots$*.*

Proof. Matrix $\mathbf{P}^{(t+1)}$ takes the form:

$$\mathbf{P}^{(t+1)} = \mathbf{P}^{(t)} - \frac{K}{\Gamma(\alpha-1)}\left(\sum_{r=0}^{t-1} V_\alpha^2(t-r+1)\sin\mathbf{X}^{(r)} + \sin\mathbf{X}^{(t)}\right). \tag{52}$$

Firstly:

$$\mathbf{P}^{(t)} = \rho_{0,p}^{(t)}\mathbf{I} + \sum_{j=1}^{n-1}\mu_{j,p}^{(t)}\mathbf{N}_j. \tag{53}$$

Secondly:

$$\begin{aligned}
&\sum_{r=0}^{t-1} V_\alpha^2(t-r+1)\sin\mathbf{X}^{(r)}\\
&= \sum_{r=0}^{t-1} V_\alpha^2(t-r+1)\left(\sin\left(\rho_{0,x}^{(r)}\right)\mathbf{I} + \sum_{j=1}^{n-1}\left(\sum_{m=1}^{j}\frac{\sin\left(\rho_{0,x}^{(r)}+\frac{m\pi}{2}\right)}{m!}\sum_{\substack{i_1+i_2+\cdots+i_m=j\\ i_1,i_2,\ldots,i_m\geq 1}}\mu_{i_1,x}^{(r)}\mu_{i_2,x}^{(r)}\cdots\mu_{i_m,x}^{(r)}\right)\mathbf{N}_j\right)\\
&= \left(\sum_{r=0}^{t-1} V_\alpha^2(t-r+1)\sin\left(\rho_{0,x}^{(r)}\right)\right)\mathbf{I}\\
&\quad + \left(\sum_{r=0}^{t-1} V_\alpha^2(t-r+1)\sum_{j=1}^{n-1}\left(\sum_{m=1}^{j}\frac{\sin\left(\rho_{0,x}^{(r)}+\frac{m\pi}{2}\right)}{m!}\sum_{\substack{i_1+i_2+\cdots+i_m=j\\ i_1,i_2,\ldots,i_m\geq 1}}\mu_{i_1,x}^{(r)}\mu_{i_2,x}^{(r)}\cdots\mu_{i_m,x}^{(r)}\right)\right)\mathbf{N}_j\\
&= \left(\sum_{r=0}^{t-1} V_\alpha^2(t-r+1)\sin\left(\rho_{0,x}^{(r)}\right)\right)\mathbf{I}\\
&\quad + \sum_{j=1}^{n-1}\left(\sum_{r=0}^{t-1} V_\alpha^2(t-r+1)\left(\sum_{m=1}^{j}\frac{\sin\left(\rho_{0,x}^{(r)}+\frac{m\pi}{2}\right)}{m!}\sum_{\substack{i_1+i_2+\cdots+i_m=j\\ i_1,i_2,\ldots,i_m\geq 1}}\mu_{i_1,x}^{(r)}\mu_{i_2,x}^{(r)}\cdots\mu_{i_m,x}^{(r)}\right)\right)\mathbf{N}_j.
\end{aligned} \tag{54}$$

Thirdly:

$$\sin\left(\mathbf{X}^{(t)}\right) = \sin\left(\rho_{0,x}^{(t)}\right)\mathbf{I} + \sum_{j=1}^{n-1}\left(\sum_{m=1}^{j}\frac{\sin\left(\rho_{0,x}^{(t)}+\frac{m\pi}{2}\right)}{m!}\sum_{\substack{i_1+i_2+\cdots+i_m=j\\ i_1,i_2,\ldots,i_m\geq 1}}\mu_{i_1,x}^{(t)}\mu_{i_2,x}^{(t)}\cdots\mu_{i_m,x}^{(t)}\right)\mathbf{N}_j. \tag{55}$$

Therefore, the matrix $\mathbf{P}^{(t+1)}$ is still a nilpotent matrix with:

$$\begin{aligned}
\rho_{0,p}^{(t+1)} &= \rho_{0,p}^{(t)} - \frac{K}{\Gamma(\alpha-1)}\left[\sum_{r=0}^{t-1} V_\alpha^2(t-r+1)\sin\left(\rho_{0,x}^{(r)}\right) + \sin\left(\rho_{0,x}^{(t)}\right)\right], \quad (\mathrm{mod}\,2\pi),\\
\mu_{j,p}^{(t+1)} &= \mu_{j,p}^{(t)} - \frac{K}{\Gamma(\alpha-1)}\left[\sum_{r=0}^{t-1} V_\alpha^2(t-r+1)\left(\sum_{m=1}^{j}\frac{\sin\left(\rho_{0,x}^{(r)}+\frac{m\pi}{2}\right)}{m!}\sum_{\substack{i_1+i_2+\cdots+i_m=j\\ i_1,i_2,\ldots,i_m\geq 1}}\mu_{i_1,x}^{(r)}\mu_{i_2,x}^{(r)}\cdots\mu_{i_m,x}^{(r)}\right)\right.\\
&\qquad \left. + \sum_{m=1}^{j}\frac{\sin\left(\rho_{0,x}^{(t)}+\frac{m\pi}{2}\right)}{m!}\sum_{\substack{i_1+i_2+\cdots+i_m=j\\ i_1,i_2,\ldots,i_m\geq 1}}\mu_{i_1,x}^{(t)}\mu_{i_2,x}^{(t)}\cdots\mu_{i_m,x}^{(t)}\right],
\end{aligned} \tag{56}$$

$j = 1, 2, \ldots, n-1.$

It is important to note that when $t = 0$, the sum $\sum_{r=0}^{t-1} = \sum_{r=0}^{-1}$ in the recursions for $\rho_{0,p}^{(1)}$ and $\mu_{j,p}^{(1)}$ is an empty sum, which by convention equals zero. Therefore, at $t = 0$, the recursion reduces to:

$$\begin{aligned}
\rho_{0,p}^{(1)} &= \rho_{0,p}^{(0)} - \frac{K}{\Gamma(\alpha-1)} \sin\left(\rho_{0,x}^{(0)}\right), \quad (\mathrm{mod}\, 2\pi), \\
\mu_{j,p}^{(1)} &= \mu_{j,p}^{(0)} - \frac{K}{\Gamma(\alpha-1)} \sum_{m=1}^{j} \frac{\sin\left(\rho_{0,x}^{(0)} + \frac{m\pi}{2}\right)}{m!} \sum_{\substack{i_1+\cdots+i_m=j \\ i_1,\ldots,i_m \geq 1}} \mu_{i_1,x}^{(0)} \cdots \mu_{i_m,x}^{(0)},
\end{aligned} \tag{57}$$

which is well defined and consistent with the initial conditions.

Note that the summation over m in the update of $\mu_{j,p}^{(t+1)}$ starts at $m = 1$ rather than $m = 0$. The $m = 0$ term in the Taylor series expansion of $\sin\left(\mathbf{X}^{(r)}\right)$ produces $\sin\left(\rho_{0,x}^{(r)}\right)\mathbf{I}$, which is a scalar multiple of the identity matrix $\mathbf{I}$. Since $\mathbf{I}$ and $\mathbf{N}_j$ are linearly independent, this term contributes exclusively to the update of the scalar coefficient $\rho_{0,p}^{(t+1)}$ and not to the updates of the nilpotent coefficients $\mu_{j,p}^{(t+1)}$. Therefore, the $m = 0$ term is correctly excluded from the μ update.

It is important to note that the modulo 2π operation is not applied to the auxiliary parameters $\mu_{j,p}^{(t)}$. This is a deliberate choice. The scalar eigenvalue $\rho_{0,p}^{(t)}$ represents a phase variable defined on the circle, and the modulo operation preserves its physical interpretation. The auxiliary parameters $\mu_{j,p}^{(t)}$, in contrast, are algebraic coefficients of the nilpotent components of the matrix. Their growth without bound is not a numerical artifact but a genuine mathematical phenomenon produced by the nilpotent algebraic structure. Applying a modulo operation to $\mu_{j,p}^{(t)}$ would artificially suppress this blow-up effect and would eliminate the hierarchical Arnold tongue structures that are the central subject of this paper.

Matrix $\mathbf{X}^{(t+1)}$ takes the following form:

$$\mathbf{X}^{(t+1)} = \mathbf{X}^{(t)} + \mathbf{P}^{(0)} - \frac{K}{\Gamma(\alpha)} \sum_{r=0}^{t} V_\alpha^1(t-r+1) \sin \mathbf{X}^{(r)}. \tag{58}$$

Firstly:

$$\mathbf{X}^{(t)} = \rho_{0,x}^{(t)}\mathbf{I} + \sum_{j=1}^{n-1} \mu_{j,x}^{(t)} \mathbf{N}_j. \tag{59}$$

Secondly:

$$\mathbf{P}^{(0)} = \rho_{0,p}^{(0)}\mathbf{I} + \sum_{j=1}^{n-1} \mu_{j,p}^{(0)} \mathbf{N}_j. \tag{60}$$

Thirdly:

$$\begin{aligned}
&\sum_{r=0}^{t} V_\alpha^1(t-r+1) \sin \mathbf{X}^{(r)} \\
&= \left(\sum_{r=0}^{t} V_\alpha^1(t-r+1) \sin\left(\rho_{0,x}^{(r)}\right) \right) \mathbf{I} \\
&\quad + \sum_{j=1}^{n-1} \left(\sum_{r=0}^{t} V_\alpha^1(t-r+1) \left(\sum_{m=1}^{j} \frac{\sin\left(\rho_{0,x}^{(r)} + \frac{m\pi}{2}\right)}{m!} \sum_{\substack{i_1+i_2+\cdots+i_m=j \\ i_1,i_2,\ldots,i_m \geq 1}} \mu_{i_1,x}^{(r)} \mu_{i_2,x}^{(r)} \cdots \mu_{i_m,x}^{(r)} \right) \right) \mathbf{N}_j.
\end{aligned} \tag{61}$$

Therefore, the matrix $\mathbf{X}^{(t+1)}$ is still a nilpotent matrix with:

$$\begin{aligned}
\rho_{0,x}^{(t+1)} &= \rho_{0,x}^{(t)} + \rho_{0,p}^{(0)} - \frac{K}{\Gamma(\alpha)} \sum_{r=0}^{t} V_\alpha^1(t-r+1) \sin\left(\rho_{0,x}^{(r)}\right), \quad (\mathrm{mod}\, 2\pi), \\
\mu_{j,x}^{(t+1)} &= \mu_{j,x}^{(t)} + \mu_{j,p}^{(0)} \\
&\quad - \frac{K}{\Gamma(\alpha)} \sum_{r=0}^{t} V_\alpha^1(t-r+1) \left(\sum_{m=1}^{j} \frac{\sin\left(\rho_{0,x}^{(r)} + \frac{m\pi}{2}\right)}{m!} \sum_{\substack{i_1+i_2+\cdots+i_m=j \\ i_1,i_2,\ldots,i_m \geq 1}} \mu_{i_1,x}^{(r)} \mu_{i_2,x}^{(r)} \cdots \mu_{i_m,x}^{(r)} \right),
\end{aligned} \tag{62}$$

$j = 1, 2, \ldots, n-1$.

The partition sum over $i_1 + i_2 + \cdots + i_m = j$ with $i_1, i_2, \ldots, i_m \geq 1$ in Equation (62) arises directly from the nilpotent multiplication rule $\mathbf{N}_{i_1} \cdot \mathbf{N}_{i_2} \cdots \mathbf{N}_{i_m} = \mathbf{N}_{i_1+i_2+\cdots+i_m} = \mathbf{N}_j$, which holds whenever $i_1 + i_2 + \cdots + i_m = j \leq n-1$, and gives $\mathbf{\Theta}$ otherwise. This rule ensures that all products of nilpotent matrices contributing to the coefficient of $\mathbf{N}_j$ are exactly those whose indices sum to j. Consequently, the nilpotent structure of $\mathbf{X}^{(t+1)}$ is preserved under iteration, with the same nilpotent basis $\{\mathbf{N}_j\}_{j=1}^{n-1}$ at every time step.

The algebraic structure is preserved: all iterates of $\mathbf{P}^{(t+1)}$ remain nilpotent with the same $\mathbf{N}_j$. However, unlike the idempotent case, the coefficients are coupled through higher-order terms, leading to richer and more entangled dynamics. □

In summary, Lemma 2 establishes that the nilpotent structure of the initial matrices is preserved exactly at every iteration of the fractional standard map. The scalar coefficients $\rho_{0,p}^{(t)}$, $\rho_{0,x}^{(t)}$, $\mu_{j,p}^{(t)}$, and $\mu_{j,x}^{(t)}$ evolve according to explicit recursive relations, while the nilpotent basis $\{\mathbf{N}_j\}_{j=1}^{n-1}$ remains unchanged. The coupling between coefficients of different orders, induced by the nonlinear sine function and the fractional memory kernel, is what gives rise to the hierarchical Arnold tongue structures observed in the numerical simulations.

3.3. The Fractional Standard Map of 4×4 *Nilpotent Matrices*

Consider the fractional standard map that acts on nilpotent matrices of order $n = 4$. In this section, the corresponding computational formulas for the eigenvalues and auxiliary parameters of $\mathbf{P}^{(t+1)}$ and $\mathbf{X}^{(t+1)}$ are derived.

Let $\mathbf{P}^{(0)}$ and $\mathbf{X}^{(0)}$ be defined as:

$$\mathbf{P}^{(0)} = \rho_{0,p}^{(0)}\mathbf{I} + \mu_{1,p}^{(0)}\mathbf{N}_1 + \mu_{2,p}^{(0)}\mathbf{N}_2 + \mu_{3,p}^{(0)}\mathbf{N}_3, \quad \mathbf{X}^{(0)} = \rho_{0,x}^{(0)}\mathbf{I} + \mu_{1,x}^{(0)}\mathbf{N}_1 + \mu_{2,x}^{(0)}\mathbf{N}_2 + \mu_{3,x}^{(0)}\mathbf{N}_3, \tag{63}$$

where $\rho_{0,p}^{(0)}, \rho_{0,x}^{(0)}, \mu_{j,p}^{(0)}, \mu_{j,x}^{(0)} \in \mathbb{R}$, and the initial values of the auxiliary parameters $\mu_{1,p}^{(0)}$ and $\mu_{1,x}^{(0)}$ are not equal to 0. Then

$$\begin{aligned}
\mathbf{P}^{(t+1)} &= \rho_{0,p}^{(t+1)}\mathbf{I} + \mu_{1,p}^{(t+1)}\mathbf{N}_1 + \mu_{2,p}^{(t+1)}\mathbf{N}_2 + \mu_{3,p}^{(t+1)}\mathbf{N}_3, \\
\mathbf{X}^{(t+1)} &= \rho_{0,x}^{(t+1)}\mathbf{I} + \mu_{1,x}^{(t+1)}\mathbf{N}_1 + \mu_{2,x}^{(t+1)}\mathbf{N}_2 + \mu_{3,x}^{(t+1)}\mathbf{N}_3,
\end{aligned} \tag{64}$$

where

$$
\begin{aligned}
\rho_{0,p}^{(t+1)} &= \rho_{0,p}^{(t)} - \frac{K}{\Gamma(\alpha-1)}\left[\sum_{r=0}^{t-1} V_\alpha^2(t-r+1)\sin\left(\rho_{0,x}^{(r)}\right) + \sin\left(\rho_{0,x}^{(t)}\right)\right], \pmod{2\pi},\\
\mu_{1,p}^{(t+1)} &= \mu_{1,p}^{(t)} - \frac{K}{\Gamma(\alpha-1)}\left[\sum_{r=0}^{t-1} V_\alpha^2(t-r+1)\mu_{1,x}^{(r)}\cos\left(\rho_{0,x}^{(r)}\right) + \mu_{1,x}^{(t)}\cos\left(\rho_{0,x}^{(t)}\right)\right],\\
\mu_{2,p}^{(t+1)} &= \mu_{2,p}^{(t)} - \frac{K}{\Gamma(\alpha-1)}\left[\sum_{r=0}^{t-1} V_\alpha^2(t-r+1)\left(\mu_{2,x}^{(r)}\cos\left(\rho_{0,x}^{(r)}\right) - \frac{\left(\mu_{1,x}^{(r)}\right)^2\sin\left(\rho_{0,x}^{(r)}\right)}{2}\right)\right.\\
&\qquad\left. + \mu_{2,x}^{(t)}\cos\left(\rho_{0,x}^{(t)}\right) - \frac{\left(\mu_{1,x}^{(t)}\right)^2\sin\left(\rho_{0,x}^{(t)}\right)}{2}\right],\\
\mu_{3,p}^{(t+1)} &= \mu_{3,p}^{(t)} - \frac{K}{\Gamma(\alpha-1)}\left[\sum_{r=0}^{t-1} V_\alpha^2(t-r+1)\left(\mu_{3,x}^{(r)}\cos\left(\rho_{0,x}^{(r)}\right) - \mu_{1,x}^{(r)}\cdot\mu_{2,x}^{(r)}\sin\left(\rho_{0,x}^{(r)}\right) - \frac{\left(\mu_{1,x}^{(r)}\right)^3\cos\left(\rho_{0,x}^{(r)}\right)}{6}\right)\right.\\
&\qquad\left. + \mu_{3,x}^{(t)}\cos\left(\rho_{0,x}^{(t)}\right) - \mu_{1,x}^{(t)}\cdot\mu_{2,x}^{(t)}\sin\left(\rho_{0,x}^{(t)}\right) - \frac{\left(\mu_{1,x}^{(t)}\right)^3\cos\left(\rho_{0,x}^{(t)}\right)}{6}\right],\\
\rho_{0,x}^{(t+1)} &= \rho_{0,x}^{(t)} + \rho_{0,p}^{(0)} - \frac{K}{\Gamma(\alpha)}\sum_{r=0}^{t} V_\alpha^1(t-r+1)\sin\left(\rho_{0,x}^{(r)}\right), \pmod{2\pi},\\
\mu_{1,x}^{(t+1)} &= \mu_{1,x}^{(t)} + \mu_{1,p}^{(0)} - \frac{K}{\Gamma(\alpha)}\sum_{r=0}^{t} V_\alpha^1(t-r+1)\mu_{1,x}^{(r)}\cos\rho_{0,x}^{(r)},\\
\mu_{2,x}^{(t+1)} &= \mu_{2,x}^{(t)} + \mu_{2,p}^{(0)} - \frac{K}{\Gamma(\alpha)}\sum_{r=0}^{t} V_\alpha^1(t-r+1)\left(\mu_{2,x}^{(r)}\cos\left(\rho_{0,x}^{(r)}\right) - \frac{\left(\mu_{1,x}^{(r)}\right)^2\sin\left(\rho_{0,x}^{(r)}\right)}{2}\right),\\
\mu_{3,x}^{(t+1)} &= \mu_{3,x}^{(t)} + \mu_{3,p}^{(0)} - \frac{K}{\Gamma(\alpha)}\sum_{r=0}^{t} V_\alpha^1(t-r+1)\left(\mu_{3,x}^{(r)}\cos\left(\rho_{0,x}^{(r)}\right) - \mu_{1,x}^{(r)}\cdot\mu_{2,x}^{(r)}\sin\left(\rho_{0,x}^{(r)}\right) - \frac{\left(\mu_{1,x}^{(r)}\right)^3\cos\left(\rho_{0,x}^{(r)}\right)}{6}\right),
\end{aligned}
\tag{65}
$$

$t = 0, 1, \ldots$.

In summary, Section 3.3 provides the explicit computational formulas for the fractional standard map of 4×4 nilpotent matrices. The recursive relations for $\mu_{1,x}^{(t+1)}$, $\mu_{2,x}^{(t+1)}$, and $\mu_{3,x}^{(t+1)}$ reveal the hierarchical coupling structure in concrete form: $\mu_{1,x}^{(t)}$ evolves independently, $\mu_{2,x}^{(t)}$ is driven by the quadratic term $\left(\mu_{1,x}^{(t)}\right)^2$, and $\mu_{3,x}^{(t)}$ is driven by both the cubic term $\left(\mu_{1,x}^{(t)}\right)^3$ and the mixed product $\mu_{1,x}^{(t)}\cdot\mu_{2,x}^{(t)}$. These explicit formulas form the computational backbone of the numerical simulations presented in Section 5.

3.4. The Computational Scheme for $\mu_{1,x}^{(t+1)}$, $\mu_{2,x}^{(t+1)}$, and $\mu_{3,x}^{(t+1)}$

As discussed in [59], the patterns of Arnold tongues are constructed from sequences of the auxiliary parameter $\mu_{1,x}^{(t)}$. Nilpotent matrices of order 4 generate three hierarchies of auxiliary parameters $\mu_{1,x}^{(t+1)}$, $\mu_{2,x}^{(t+1)}$, and $\mu_{3,x}^{(t+1)}$ (65).

Figure 1 presents a schematic diagram for the iterative construction of the auxiliary parameter $\mu_{1,x}^{(t+1)}$ ($t = 0, 1, 2$) as defined by (65). The diagram shows the explicit construction of $\mu_{1,x}^{(t+1)}$ only. The constructions for $\mu_{2,x}^{(t+1)}$ and $\mu_{3,x}^{(t+1)}$ are in principle analogous, but involve additional higher-order nilpotent couplings.

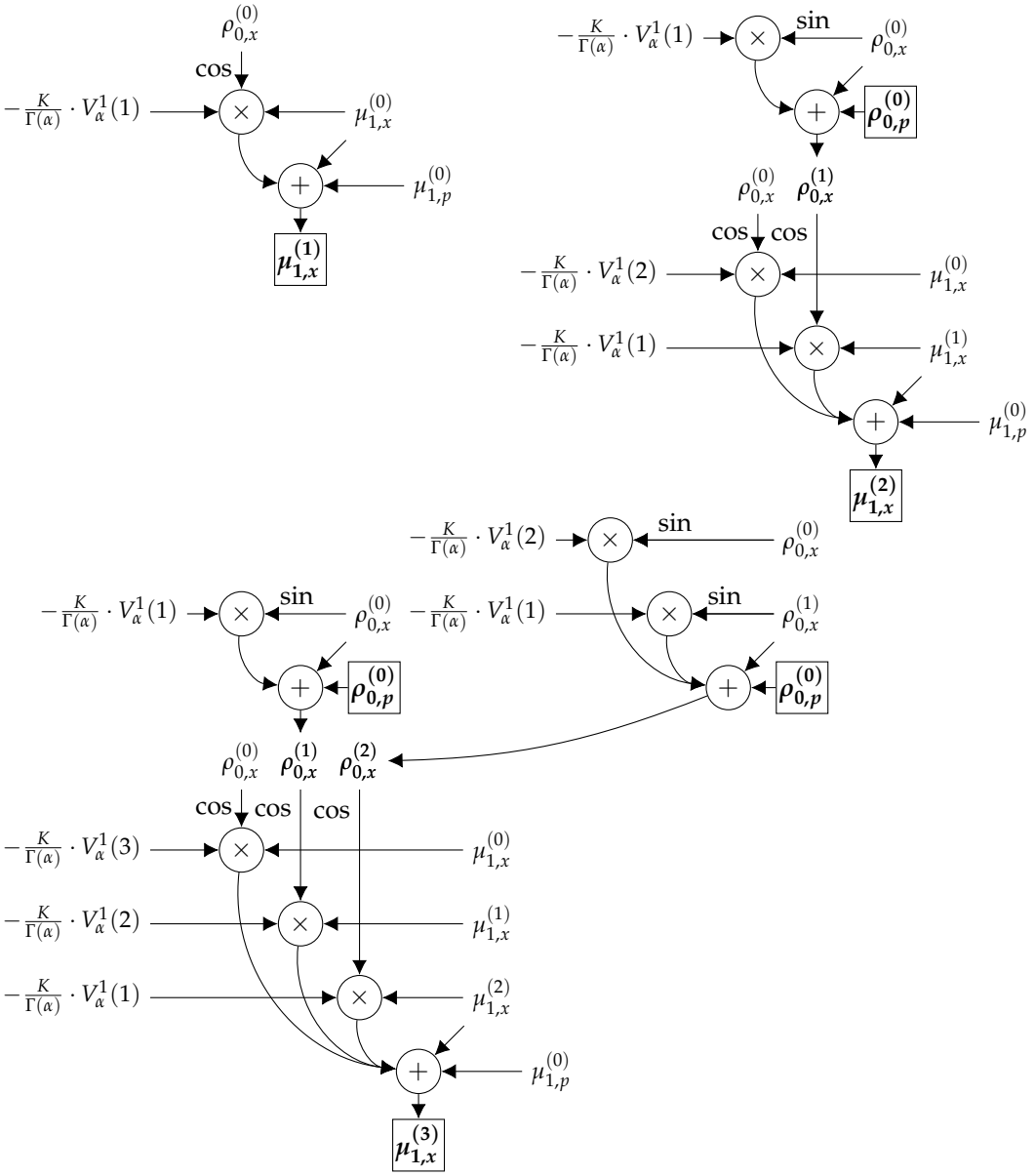

Figure 1. A schematic diagram illustrating the iterative construction of the auxiliary parameter $\mu_{1,x}^{(t+1)}$ for $t = 0, 1, 2$. The auxiliary parameters are scalar coefficients of the nilpotent components of the matrix state, and their iterative update encodes the long-memory effects of the fractional derivative. Each level incorporates cosine-modulated multiplicative interactions and additive contributions from all preceding levels, reflecting the cumulative influence of the entire history of the dynamical system. Analogous schemes hold for $\mu_{2,x}^{(t+1)}$ and $\mu_{3,x}^{(t+1)}$.

Figure 1 illustrates the first three steps of the iterative process, emphasizing the algebraic structure induced by the nilpotent matrix framework. Each block represents an elementary arithmetic operation. The circles marked with "$\times$" denote multiplications involving the cosine modulation terms $\cos\left(\rho_{0,x}^{(t)}\right)$, while the circles marked with "$+$" represent the additive accumulation of contributions from lower-order components. The directional arrows indicate the flow of information between successive layers.

At the first level, the component $\mu_{1,x}^{(1)}$ is obtained by multiplying the base eigenvalue by the corresponding cosine modulation term and then adding the initial contribution from the p-component. This step represents the primary dynamical activation of the x-component and reflects the nonlinear forcing inherent in the fractional standard map.

At the second level, the construction of $\mu_{1,x}^{(2)}$ becomes coupled. Two multiplicative channels are present, and their outputs are combined additively. At this stage, the nilpotent structure begins to manifest explicitly: higher-order components depend on both newly generated cosine-modulated terms and outputs inherited from the previous level. Thus, the components $\mu_{1,x}^{(t+1)}$ are not formed independently but arise through a hierarchical transformation of the previous contributions.

At the third level, the hierarchical architecture becomes more pronounced. Three cosine-modulated multiplicative channels appear, inputs from all preceding levels contribute, and the resulting terms converge additively to produce the output. This stage clearly exhibits the nilpotent structure: each higher-order component accumulates transformed contributions from all lower-order levels.

The computational diagram in Figure 1 clearly illustrates the effect of fractional memory, whose memory horizon extends back to the initial condition. The terms $V_{\alpha}^{s}(t-j+1)$ encode this fractional memory contribution explicitly. In fact, they arise from the discrete Caputo operator and possess a nonlocal convolution structure: each value is formed as a weighted sum over all past states, with power-law-type memory kernels determined by the fractional order α. Consequently, the present state depends not only on the immediately preceding iterate but also on the entire history of the process.

Importantly, the quantities $V_{\alpha}^{s}(t-j+1)$ can be computed independently prior to executing the iterative procedure that constructs the sequence of auxiliary parameters $\mu_{1,x}^{(t+1)}$ (see Figure 1). The diagram, therefore, separates the nonlocal memory accumulation from the subsequent algebraic (nilpotent) coupling mechanism.

Analogous (though progressively more intricate) computational schemes arise for the parameters $\mu_{2,x}^{(t+1)}$ and $\mu_{3,x}^{(t+1)}$.

4. The Calibration of the Numerical Scheme

4.1. The H-Rank Algorithm

The H-rank algorithm is a concise and computationally efficient tool for evaluating the algebraic complexity of sequences produced by discrete or continuous dynamical systems [65,66]. The concept of H-rank was introduced in [67] as the number of singular values of the catalectic Hankel matrix (constructed from the given time series) that exceed a prescribed threshold.

The H-rank algorithm uses two parameters: the size of the Hankel matrix h and the threshold ε. The parameter h defines the size of the observation window $L = 2h - 1$ and the observable range of H-ranks $[0, h]$. The threshold ε determines whether the algorithm overshoots or undershoots the dynamics in the current observation window. A careful calibration of both parameters is required before any further investigations [49].

4.2. The Calibration of h and ε in the H-Rank Algorithm

The calibration of the parameters of the H-rank algorithm is performed for the first hierarchical layer of the auxiliary parameter $\mu_{1,x}^{(t)}$ (the order of the nilpotent matrices is set to 2).

The range of the initial phase $\rho_{0,p}^{(0)}$ is set to the interval $[0, 2\pi]$; the nonlinearity parameter K to $[0, 2]$; and the fractionality parameter α to 1.001 [59]. For each individual value of $\rho_{0,p}^{(0)}$ and K, the initial conditions $\mu_{1,x}^{(0)}$ and $\mu_{1,p}^{(0)}$ are set to 1 and $\rho_{0,x}^{(0)}$ is set to 0 [59], and the algorithm depicted in Figure 2 is executed for 399 iterations (resulting in a maximal H-rank equal to 200). The H-rank patterns are visualized using a blue-yellow color map, where blue corresponds to H-rank 0 and yellow corresponds to the maximal H-rank of 200.

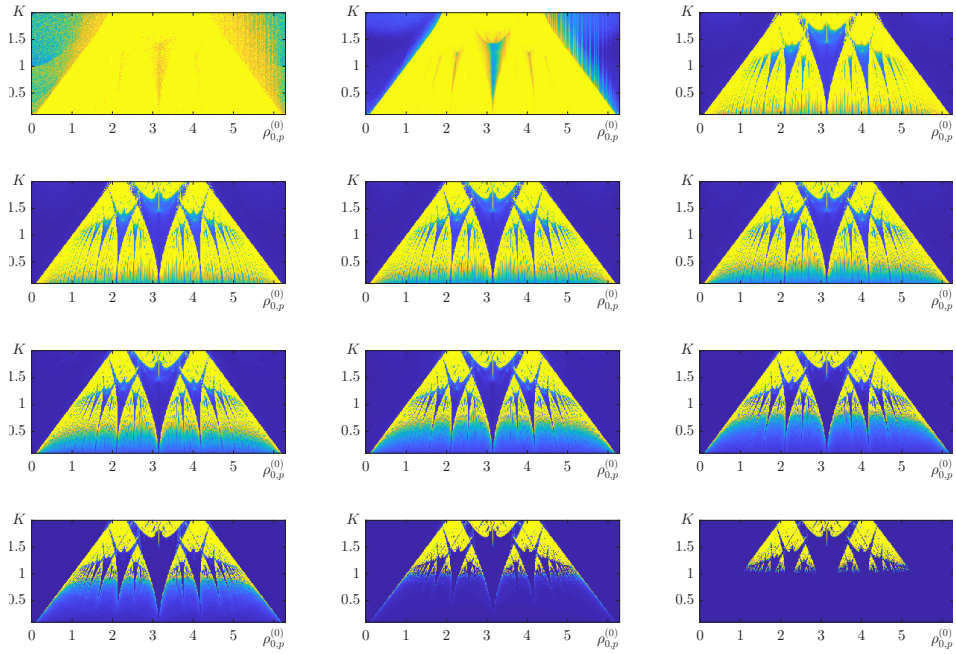

Figure 2. H-rank parameter maps computed for twelve values of the threshold parameter $\varepsilon \in (10^{-16}, 10^{-14}, 10^{-12}, 10^{-10}, 10^{-8}, 10^{-6}, 10^{-4}, 10^{-2}, 1, 50, 5000, 10^{6})$ in the parameter plane $\left(\rho_{0,p}^{(0)}, K\right)$. The H-rank is a measure of the algebraic complexity of a dynamical sequence, computed as the number of significant singular values of a Hankel matrix constructed from the sequence. The horizontal axis corresponds to the initial phase parameter $\rho_{0,p}^{(0)}$ and the vertical axis to the nonlinearity parameter K. Dark blue corresponds to H-rank 0 and light yellow corresponds to H-rank 200. For very small values of ε, almost all grid points are assigned the maximum H-rank, resulting in a predominantly yellow map. For very large values of ε, almost all grid points are assigned H-rank 0, resulting in a predominantly blue map. The Arnold tongue structures are most clearly visible in the intermediate range of ε values, where a balanced distribution between yellow and blue regions is achieved. This confirms that the observed hierarchical structures are not an artifact of the threshold selection.

The parameter ε in the H-rank algorithm must be calibrated. If ε is too small (for example, 10^{-16}), the entire map becomes yellow (Figure 2). If ε is too large (for example, 10^{6}), the map becomes predominantly blue (Figure 2). Only intermediate values of ε produce a balanced distribution of H-ranks.

The H-rank patterns in Figure 2 reveal the well-recognizable structure of Arnold tongues in the parameter plane $(\rho_{0,p}^{(0)}, K)$. The calibration strategy for the parameter ε is based on the requirement that, within the trapezoidal region occupied by the Arnold tongues, 50% of the pixels have H-ranks greater than 100, while the remaining 50% have H-ranks lower than 100.

Twelve panels in Figure 2 show the patterns of H-ranks computed at $\varepsilon = 10^{-16}$, 10^{-14}, 10^{-12}, 10^{-10}, 10^{-8}, 10^{-6}, 10^{-4}, 10^{-2}, 1, 50, 5000, and 10^{6}. The percentages of pixels with H-ranks greater than 100 for different values of ε are depicted in Figure 3. Note that the horizontal axis in Figure 3 is logarithmic.

The dashed black line in Figure 3 represents the linear approximation of the percentages of pixels with H-ranks greater than 100 as a function of ε: $y = -1.8x + 40$, where $x = \ln(\varepsilon)$. The near-linear trend on the logarithmic scale suggests that the contraction of the area occupied by pixels with H-ranks greater than 100 follows an approximately logarithmic scaling law. The calibration objective is to determine the value of ε for which the two zones (H-ranks greater than and lower than 100) occupy equal areas. The intersection of the red horizontal line with the inclined black line yields $x = -9\frac{4}{9}$, which corresponds to $\varepsilon = 7.92 \cdot 10^{-5}$. This value of ε is used in all subsequent computations.

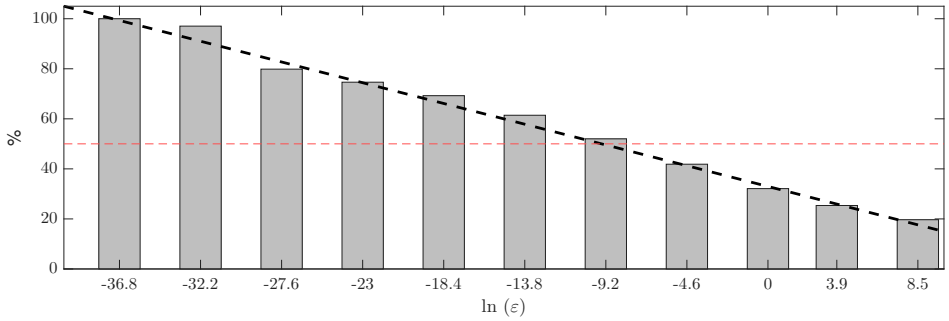

Figure 3. The percentage of grid points with H-rank exceeding 100 as a function of $\ln(\varepsilon)$. Each bar represents the proportion of grid points for which the H-rank exceeds 100, serving as a measure of how much of the parameter plane exhibits high algebraic complexity. The red dashed horizontal line marks the 50% threshold, which corresponds to a perfectly balanced distribution between high and low H-rank regions in the parameter map and serves as the calibration criterion for the H-rank algorithm. The black dashed line shows the linear approximation $y = -1.8x + 33$ fitted to the bar values, confirming that the percentage decreases smoothly and monotonically as ε increases. The logarithmic scale is used because ε spans several orders of magnitude, ranging from 10^{-16} to 10^{6}. The calibration is performed on the first hierarchical layer only, and the resulting value of ε is then applied consistently to all higher layers, enabling direct qualitative and quantitative comparison across the hierarchy.

The H-rank of a sequence is computed from the singular values of a 200×200 Hankel matrix. The minimum possible H-rank is 0, corresponding to a trivially simple sequence, and the maximum is 200, corresponding to maximum algebraic complexity. In the parameter maps, dark blue corresponds to H-rank 0 and light yellow corresponds to H-rank 200.

The 50% threshold means that exactly half of the grid points in the parameter map have an H-rank greater than 100. This produces a perfectly balanced color distribution between dark blue and light yellow. It is the natural midpoint between the two extremes, analogous to choosing the midpoint of a grayscale in image processing.

The sensitivity of the results with respect to the threshold parameter ε is demonstrated in Figure 2, which shows the H-rank parameter maps for 12 values of ε spanning the range from 10^{-16} to 10^{6}. The qualitative structure of the Arnold tongues is robust over a wide intermediate range of ε values. Figure 3 shows that the proportion of high H-rank points decreases smoothly and nearly linearly as a function of $\ln(\varepsilon)$, and the 50% threshold corresponds to a well-defined and stable point on this curve.

The calibration is performed on the first hierarchical layer only. The resulting value of ε is then applied consistently to all higher hierarchical layers without any further adjustment. This ensures that the color distributions across different layers are directly comparable, both qualitatively and quantitatively. Any deviation from the balanced color distribution in higher layers directly reflects a genuine change in the dynamical complexity of the system, not an artifact of the calibration procedure.

5. Computational Simulations

5.1. The Hierarchies of Arnold Tongues of Divergence

The calibrated H-rank technique is used to visualize three patterns corresponding to $\mu_{1,x}^{(t)}$ (panel A), $\mu_{2,x}^{(t)}$ (panel B), and $\mu_{3,x}^{(t)}$ (panel C) in the parameter plane $(\rho_{0,p}^{(0)}, K)$ (Figure 4).

Arnold-type tongue structures are clearly visible in all three panels of Figure 4. However, the average algebraic complexity of the trajectories associated with $\mu_{3,x}^{(t)}$ is higher than that of $\mu_{2,x}^{(t)}$ and $\mu_{1,x}^{(t)}$. This increase in complexity is reflected by the growing dominance of the yellow color in panel C. In addition, the fine structure of the pattern gradually changes across the panels, becoming more intricate at higher orders. The H-rank algorithm is

calibrated so that panel A produces approximately equal proportions of yellow and blue regions, providing a reference level for comparison across the panels.

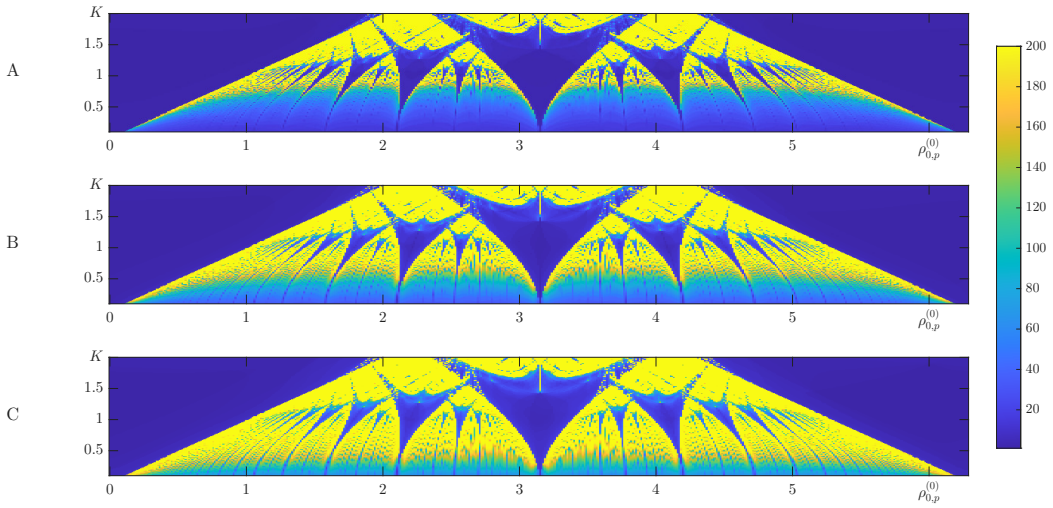

Figure 4. Patterns of $\mu_{1,x}^{(t)}$ panel (**A**), $\mu_{2,x}^{(t)}$ panel (**B**), and $\mu_{3,x}^{(t)}$ panel (**C**) obtained using the calibrated H-rank algorithm in the parameter plane $(\rho_{0,p}^{(0)}, K)$, where $\rho_{0,p}^{(0)}$ is the initial phase parameter and K is the nonlinearity parameter. The auxiliary parameters $\mu_{j,x}^{(t)}$ are scalar coefficients of the nilpotent components of the matrix state, and their algebraic complexity reflects the richness of the transient dynamics at each hierarchical level. Dark blue corresponds to H-rank 0 and light yellow corresponds to H-rank 200. Arnold-type tongue structures are visible in all panels. As the hierarchical order increases, the average algebraic complexity of the transient processes grows, which is reflected by the increasing dominance of yellow regions and by progressive changes in the fine structure of the pattern. The H-rank algorithm is calibrated such that panel A contains approximately equal proportions of yellow and blue regions. The same value of ε is then applied to panels (**B**,**C**), enabling direct qualitative and quantitative comparisons of the algebraic complexity across the hierarchical layers.

All numerical simulations were implemented in MATLAB (MathWorks, R2024b) and executed on a high-performance workstation equipped with an AMD Ryzen 9 5900X 12-core processor (3.7 GHz), 128 GB of DDR4 RAM (2400 MHz), and an NVIDIA GeForce RTX 3090 GPU (24 GB VRAM), running a 64-bit Windows operating system. The parameter space was discretized as a uniform 1000×1000 grid over the ranges $\rho_{0,p}^{(0)} \in [0, 2\pi]$ and $K \in [0.1, 2]$, with each trajectory integrated for $t = 1000$ iterations. The dominant computational cost arises from the convolution-type summations inherent to the Caputo fractional operator: at each iteration step t, the update requires summing over all previous states, resulting in $\mathcal{O}(t^2)$ operations per trajectory. For the full 1000×1000 grid, the total wall-clock time was approximately 6 h. The H-rank was computed using the singular value decomposition of the Hankel matrix constructed from each trajectory, with observation window $V/2 = 200$ and threshold $\varepsilon = 7.92 \times 10^{-5}$ (see Section 4 for calibration details).

5.2. The Role of the Hierarchical Layers of $\mu_{j,x}^{(t)}$

Figures 5 and 6 illustrate how the hierarchical patterns obtained with the calibrated H-rank algorithm relate to the algebraic complexity of transient processes. In both figures, the upper panels show zoomed regions of the parameter plane $(\rho_{0,p}^{(0)}, K)$ corresponding to $\mu_{1,x}^{(t)}$, $\mu_{2,x}^{(t)}$, and $\mu_{3,x}^{(t)}$. The white circles indicate the same parameter point in all panels.

In Figure 5 the selected point lies within the blue region in all three hierarchical layers. Consequently, the transient dynamics of $\mu_{1,x}^{(t)}$, $\mu_{2,x}^{(t)}$, and $\mu_{3,x}^{(t)}$ exhibit comparable algebraic complexity. This is confirmed in the lower panel, where the functions $\ln \left|\mu_{j,x}^{(t)}\right|; j = 1, 2, 3$ grow with t in a similar manner. Although their amplitudes differ (reflecting the nilpotent

hierarchy), their slopes and oscillatory regimes remain strongly correlated. Higher layers amplify the same instability mechanism rather than introducing independent dynamics.

Figure 6 demonstrates a different situation. Although the same parameter point is considered in all panels, it belongs to different color regions in different hierarchical layers: the point lies in a blue region for $\mu_{1,x}^{(t)}$, in a light-blue region for $\mu_{2,x}^{(t)}$, and in a yellow region for $\mu_{3,x}^{(t)}$. Consequently, the algebraic complexity of the corresponding transient processes increases from $\mu_{1,x}^{(t)}$ to $\mu_{3,x}^{(t)}$. The lower panel confirms this behavior, showing progressively stronger fluctuations in $\ln\left|\mu_{j,x}^{(t)}\right|$ for higher j. Now, the nilpotent hierarchy does not amplify a single coherent instability mechanism.

This example highlights an important property of the hierarchical structure. A given point in the parameter plane may belong to regions of different colors in different hierarchical layers. Therefore, the hierarchical level associated with a particular $\mu_{j,x}^{(t)}$ becomes an essential parameter to determine the algebraic complexity of the transient dynamics. In applications where such transient processes are used to encode information, the hierarchical layer can thus serve as an additional security parameter.

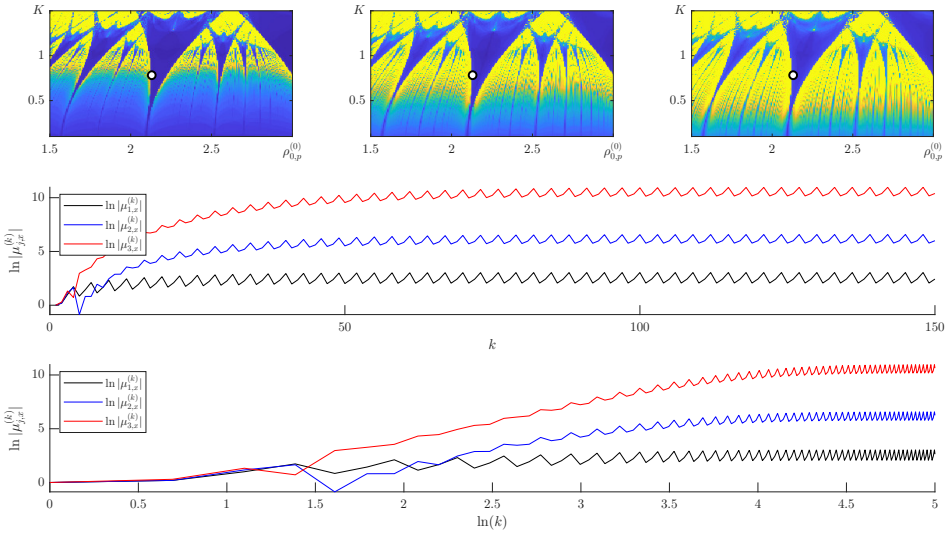

Figure 5. Zoomed regions of the parameter plane $(\rho_{0,p}^{(0)}, K)$ for $\mu_{1,x}^{(t)}$ (left), $\mu_{2,x}^{(t)}$ (center), and $\mu_{3,x}^{(t)}$ (right), where $\rho_{0,p}^{(0)}$ is the initial phase parameter and K is the nonlinearity parameter. The white circles indicate the same parameter point in all panels ($\rho_{0,p} = 2.1300$; $K = 0.7828$). In this example, the point lies in the blue region of each hierarchical layer, indicating low algebraic complexity at all levels. The middle and the bottom panels show the corresponding evolution of $\ln\left|\mu_{j,x}^{(t)}\right|$ as a function of the iteration index t on a linear scale and on a logarithmic scale of t, respectively. The logarithmic scale of t is used to distinguish algebraic growth from exponential growth: a linear trend in this representation confirms power-law-type behavior characteristic of fractional systems with long memory. The approximately linear dependence of $\ln\left|\mu_{j,x}^{(t)}\right|$ on $\ln t$ is consistent with the algebraic scaling $\left|\mu_{j,x}^{(t)}\right| \sim t^{j\beta}$, where the slope increases proportionally to the hierarchical order j. This confirms that the nilpotent hierarchy amplifies the same instability mechanism rather than introducing independent dynamics.

In the $\ln t$ representation, the curves display approximately linear trends over extended intervals. This indicates power-law-type growth typical for fractional systems with memory, distinguishing the divergence mechanism from purely exponential instability.

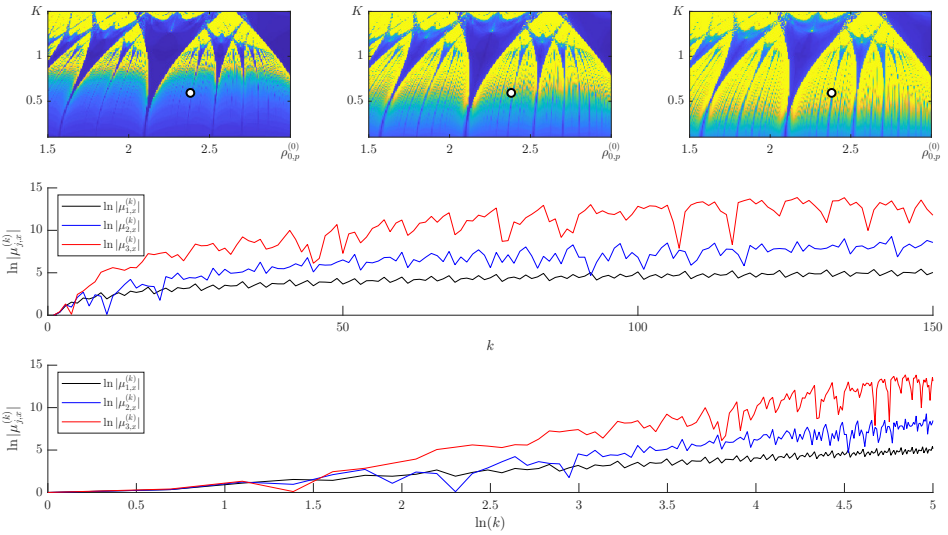

Figure 6. Same representation as in Figure 5, but for a parameter point that belongs to different color regions in different hierarchical layers ($\rho_{0,p} = 2.3813$; $K = 0.5926$). Unlike the previous example, where all three hierarchical layers showed similar dynamical complexity, here the algebraic complexity increases significantly with the hierarchical order. The point lies in the blue region for $\mu_{1,x}^{(t)}$, in a light-blue region for $\mu_{2,x}^{(t)}$, and in a yellow region for $\mu_{3,x}^{(t)}$. The fact that the same point in the parameter plane belongs to different color regions in different hierarchical layers is a direct consequence of the calibration strategy: since the same value of ε is applied consistently across all layers, the color differences reflect genuine changes in the algebraic complexity of the transient dynamics rather than artifacts of the threshold selection. The middle and the bottom panels confirm this interpretation, showing progressively stronger growth of $\ln\left|\mu_{j,x}^{(t)}\right|$ with increasing hierarchical order. This example illustrates that the hierarchical level associated with a particular $\mu_{j,x}^{(t)}$ is an essential parameter for determining the algebraic complexity of the transient dynamics, and highlights the richer dynamical behavior that emerges in the high-dimensional nilpotent setting compared to the scalar case.

5.3. The Divergence Rates of $\mu_{j,x}^{(t)}$

Let us investigate the general form of the auxiliary variable $\mu_{j,x}^{(t+1)}$ (62):

$$\mu_{j,x}^{(t+1)} = \mu_{j,x}^{(t)} + \mu_{j,p}^{(0)} - \frac{K}{\Gamma(\alpha)} \sum_{r=0}^{t} V_{\alpha}^{1}(t-r+1) \left(\sum_{m=1}^{j} \frac{\sin\left(\rho_{0,x}^{(r)} + \frac{m\pi}{2}\right)}{m!} \sum_{\substack{i_1+\cdots+i_m=j \\ i_1,i_2,\ldots,i_m \geq 1}} \mu_{i_1,x}^{(r)} \cdots \mu_{i_m,x}^{(r)} \right). \tag{66}$$

For fixed j, the update consists of a linear term containing $\mu_{j,x}^{(r)}$ and a forcing term generated by nonlinear products of lower-order variables $\mu_{i_\ell,x}^{(r)}$, $i_\ell < j$. The forcing is determined by all partitions of the integer j.

The memory kernel $V_{\alpha}^{1}(m) = m^{\alpha-1} - (m-1)^{\alpha-1}$ satisfies the asymptotic relation [48]:

$$V_{\alpha}^{1}(m) \sim (\alpha-1)m^{\alpha-2}, \qquad m \to \infty. \tag{67}$$

This asymptotic relation follows directly from the definition $V_{\alpha}^{1}(m) = m^{\alpha-1} - (m-1)^{\alpha-1}$. Factoring out $m^{\alpha-1}$ gives:

$$V_{\alpha}^{1}(m) = m^{\alpha-1}\left(1 - \left(1 - \frac{1}{m}\right)^{\alpha-1}\right). \tag{68}$$

Applying the first-order expansion $(1-x)^{\alpha-1} \approx 1-(\alpha-1)x$ for small $x = 1/m$ as $m \to \infty$ yields:

$$V_\alpha^1(m) \approx m^{\alpha-1} \cdot \frac{\alpha-1}{m} = (\alpha-1)m^{\alpha-2}, \qquad m \to \infty, \tag{69}$$

confirming the asymptotic relation (67).

Equation (69) implies a slow power-law decay of memory weights for $1 < \alpha \leq 2$. Therefore, the evolution of $\mu_{j,x}^{(t+1)}$ also depends on the entire history of $\rho_{0,x}^{(r)}$.

For $j = 1$, the recursion reduces to the linear equation

$$\mu_{1,x}^{(t+1)} = \mu_{1,x}^{(t)} + \mu_{1,p}^{(0)} - \frac{K}{\Gamma(\alpha)} \sum_{r=0}^{t} V_\alpha^1(t-r+1)\, \mu_{1,x}^{(r)} \cos\left(\rho_{0,x}^{(r)}\right). \tag{70}$$

This relation provides the fundamental auxiliary variable that drives the higher-order terms through nonlinear products.

Note that the memory kernel values $V_\alpha^1(t-r+1)$ depend only on the fractional order α and the time indices, and not on the dynamical variables $\rho_{0,x}^{(r)}$ or $\mu_{j,x}^{(r)}$. Therefore, the entire sequence of coefficients $V_\alpha^1(1), V_\alpha^1(2), \ldots, V_\alpha^1(t+1)$ can be precomputed once before the iteration starts, using the definition $V_\alpha^1(m) = m^{\alpha-1} - (m-1)^{\alpha-1}$, without any repeated evaluation of Gamma functions or their ratios. This precomputation strategy significantly reduces the computational cost of the iteration and contributes to the efficiency of the numerical scheme.

For $j \geq 2$, the forcing term in (66) is generated by products of the form

$$\mu_{i_1,x}^{(r)} \mu_{i_2,x}^{(r)} \cdots \mu_{i_m,x}^{(r)}, \qquad i_1 + \cdots + i_m = j, \tag{71}$$

which represent all partitions of j. The dominant contribution is produced by the partition $j = 1+1+\cdots+1$ ($m = j$), yielding the highest-degree product $\left(\mu_{1,x}^{(r)}\right)^j$. Consequently, the variable $\mu_{j,x}^{(t+1)}$ is driven by $\mu_{1,x}^{(t)}$ through polynomial-type forcing of degree j.

For example, for $j = 2$, the recursion may be rewritten as

$$\mu_{2,x}^{(t+1)} = \mu_{2,x}^{(t)} + \mu_{2,p}^{(0)} - \frac{K}{\Gamma(\alpha)} \sum_{r=0}^{t} V_\alpha^1(t-r+1) \left(\mu_{2,x}^{(r)} \cos\left(\rho_{0,x}^{(r)}\right) - \frac{\left(\mu_{1,x}^{(r)}\right)^2}{2} \sin\left(\rho_{0,x}^{(r)}\right) \right). \tag{72}$$

This representation separates the linear propagation of $\mu_{2,x}$ from the quadratic forcing term $\left(\mu_{1,x}^{(r)}\right)^2$. Thus, the evolution of $\mu_{2,x}$ is controlled by the second-order dependence on $\mu_{1,x}$.

Similarly, for $j = 3$, one obtains

$$\begin{aligned} \mu_{3,x}^{(t+1)} &= \mu_{3,x}^{(t)} + \mu_{3,p}^{(0)} \\ &\quad - \frac{K}{\Gamma(\alpha)} \sum_{r=0}^{t} V_\alpha^1(t-r+1) \left(\mu_{3,x}^{(r)} \cos\left(\rho_{0,x}^{(r)}\right) - \mu_{1,x}^{(r)} \mu_{2,x}^{(r)} \sin\left(\rho_{0,x}^{(r)}\right) - \frac{\left(\mu_{1,x}^{(r)}\right)^3}{6} \cos\left(\rho_{0,x}^{(r)}\right) \right). \end{aligned} \tag{73}$$

The dependence on $\mu_{1,x}$ is explicit. It enters directly through the cubic term $\left(\mu_{1,x}^{(r)}\right)^3$ and through the mixed product $\mu_{1,x}^{(r)} \mu_{2,x}^{(r)}$. The latter introduces an indirect dependence on $\mu_{1,x}$ via $\mu_{2,x}$, which itself is forced by $\left(\mu_{1,x}^{(r)}\right)^2$.

In general, for arbitrary $j \geq 2$, the structure of (66) implies that $\mu_{j,x}^{(t+1)}$ contains forcing terms of degree up to j in $\mu_{1,x}^{(r)}$. Hence, the auxiliary variables form a growth hierarchy driven by the fundamental quantity $\mu_{1,x}^{(t)}$, where higher-order terms depend on progressively higher-degree polynomial combinations of $\mu_{1,x}$.

5.4. The Algebraic Versus Exponential Scaling of $\mu_{j,x}^{(t)}$

Consider the first auxiliary variable $\mu_{1,x}^{(t)}$. Assume that the magnitude $\left|\mu_{1,x}^{(t)}\right|$ follows the algebraic scaling:

$$\left|\mu_{1,x}^{(t)}\right| \sim t^{\beta}, \qquad \beta > 0. \tag{74}$$

This assumption is consistent with the previously established structure of the hierarchy, in which higher-order auxiliary variables appear as polynomial functions of $\mu_{1,x}^{(t)}$. From the recursive relations for the higher-order variables (see (62) and (65)), we obtain:

$$\mu_{2,x}^{(t)} \sim \left(\mu_{1,x}^{(t)}\right)^2, \qquad \mu_{3,x}^{(t)} \sim \left(\mu_{1,x}^{(t)}\right)^3, \qquad \ldots, \qquad \mu_{j,x}^{(t)} \sim \left(\mu_{1,x}^{(t)}\right)^j. \tag{75}$$

Consequently,

$$\left|\mu_{j,x}^{(t)}\right| \sim t^{j\beta}.$$

Therefore, the entire hierarchy exhibits polynomial growth.

The classical Lyapunov exponent associated with a sequence δ_t is defined as:

$$L = \lim_{t\to\infty} \ln \frac{|\delta_t|}{t}. \tag{76}$$

Applying this definition to the scaling $\mu_{1,x}^{(t)} \sim t^{\beta}$ gives $\frac{1}{t}\ln\left|\mu_{1,x}^{(t)}\right| = \frac{1}{t}\ln\left(t^{\beta}\right) = \frac{\beta \ln t}{t}$. Therefore,

$$L_1 = \lim_{t\to\infty} \frac{\ln\left|\mu_{1,x}^{(t)}\right|}{t} = 0, \tag{77}$$

since $\lim_{t\to\infty} \frac{\ln t}{t} = 0$. The same calculation applies to all higher-order variables. Using the scaling $\mu_{j,x}^{(t)} \sim t^{j\beta}$, we obtain:

$$L_j = \lim_{t\to\infty} \frac{\ln\left|\mu_{j,x}^{(t)}\right|}{t} = \lim_{t\to\infty} \frac{\ln t^{j\beta}}{t} = \lim_{t\to\infty} \frac{j\beta \ln t}{t} = 0, \tag{78}$$

where $j\beta$ is a fixed positive constant independent of t, and the limit follows directly from the standard result $\lim_{t\to\infty} \frac{\ln t}{t} = 0$.

Thus, although the auxiliary variables may grow without bound, their growth is algebraic rather than exponential. The Lyapunov exponent detects only exponential divergence, and any polynomial growth leads to a vanishing value. Consequently, computing the classical Lyapunov exponents for $\mu_{1,x}, \mu_{2,x}, \ldots, \mu_{n-1,x}$ does not provide information about their effective amplification. The entire hierarchy therefore possesses a zero Lyapunov exponent despite exhibiting nontrivial algebraic growth.

These considerations regarding the algebraic scaling of $\mu_{j,x}^{(t)}$ are supported by the computational experiments shown in Figures 5 and 6, where the dependence of $\ln\left|\mu_{j,x}^{(t)}\right|$ on $\ln t$ is well approximated by a linear relation.

5.5. Winding Numbers and Circle Map Dynamics

A central tool for characterizing the qualitative behavior of the fractional standard map is the winding number (also called the rotation number), defined as the average phase advance per iteration in the lifted (unwrapped) phase space:

$$\omega = \lim_{t\to\infty} \frac{\rho_{0,x}^{(t)}}{2\pi t}, \tag{79}$$

where $\rho_{0,x}^{(t)}$ denotes the unwrapped scalar phase trajectory [68,69]. The winding number ω provides a global characterization of the long-term dynamics: when $\omega = p/q$ is rational, the orbit is periodic and closes after exactly q iterations, the system is mode-locked to an Arnold tongue. When ω is irrational, the orbit is quasiperiodic and never exactly repeats [70].

This distinction is made visually transparent through the Poincaré circle map, in which each iterate $\rho_{0,x}^{(t)}$ mod 2π is projected as a point onto the unit circle. A mode-locked orbit produces a finite cluster of recurring points, whereas a quasiperiodic orbit generates a trajectory that densely and uniformly covers the entire circle, which a consequence of the Weyl equidistribution theorem [71].

In the fractional memory setting considered here, convergence of ω is substantially slower than in the classical case $\alpha = 2$, because the power-law memory kernel introduces long transients. This makes direct numerical computation of ω from finite trajectories sensitive to the number of iterations, and the circle map visualization serves as a robust qualitative alternative [42].

To illustrate the correspondence between the H-rank landscape and the underlying dynamical regime, two representative initial conditions are selected from the parameter plane $(\rho_{0,p}^{(0)}, K)$. The first lies within a low H-rank region (center of Arnold tongue structure in Figure 7), associated with a periodic or weakly complex orbit; its circle map reveals a small number of recurrent points, confirming mode-locking (Figure 7). The second is drawn from a high H-rank region (outside of the Arnold tongue structure in Figure 7), where the orbit densely populates the circle, consistent with quasiperiodic motion (Figure 7). This correspondence validates the H-rank as a reliable indicator of the dynamical regime: a low rank signals Arnold tongue locking, while a high rank signals quasiperiodic or complex behavior.

5.6. Signal Encryption via Hierarchical Chaotic Permutations

Real-world signals typically exhibit strong statistical dependence between adjacent samples, a property that can be exploited in signal analysis and steganographic attacks [72]. To reduce this dependence and increase the security of information concealment, data scrambling techniques based on chaotic sequences have been widely studied [73]. One of the earliest frameworks proposing chaotic systems for image and signal encryption was introduced by Fridrich [74], who established the *permutation–diffusion* architecture that underlies many subsequent methods.

Let the discrete signal to be encrypted be

$$S = \{s_1, s_2, \ldots, s_N\}. \tag{80}$$

A permutation π is constructed from a chaotic sequence $X = \{x_1, x_2, \ldots, x_N\}$ by sorting its elements in ascending order and recording the original index positions. The encrypted signal is then obtained as

$$S' = S(\pi), \qquad s'_i = s_{\pi_i}, \tag{81}$$

and the original signal is recovered by applying the inverse permutation:

$$S_{\text{rec}}(\pi_i) = s'_i, \qquad \text{or equivalently,} \qquad S_{\text{rec}} = S'\left(\pi^{-1}\right). \tag{82}$$

Permutation-based encryption possesses three properties that make chaotic sequences particularly suitable as key generators: pseudorandomness, determinism, and sensitivity to initial conditions [75,76]. The permutation destroys the local correlation between adjacent signal values so that the encrypted signal loses its structural properties and becomes statistically indistinguishable from noise.

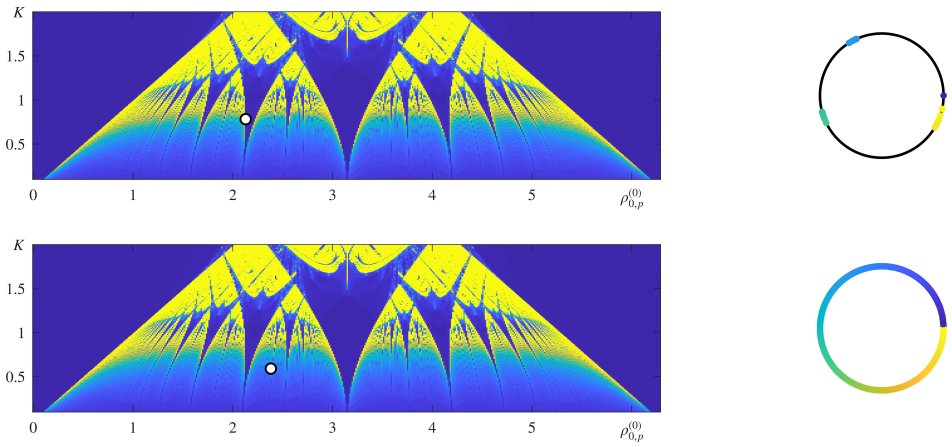

Figure 7. Winding number analysis of the fractional matrix standard map for $\alpha = 1.001$, a value close to unity at which the system approaches the classical circle map and Arnold tongue structures are most pronounced. Left panels: H-rank maps of the $\mu^{(t)}_{1,x}$ component in the parameter plane $(\rho^{(0)}_{0,p}, K)$, where $\rho^{(0)}_{0,p}$ is the initial phase parameter and K is the nonlinearity parameter. The white circle marks the selected initial condition. Right panels: Poincaré circle maps of the corresponding $\rho^{(t)}_{0,x} \mod 2\pi$ trajectory projected onto the unit circle, with point color indicating the iteration index n. The Poincaré circle map provides a visual tool for distinguishing between mode-locked and quasiperiodic orbits. A point selected from within an Arnold tongue region produces a trajectory that visits only a finite number of distinct points on the circle, indicating mode-locking to a rational rotation number. A point selected from outside an Arnold tongue region produces a trajectory that densely covers the entire circle, consistent with a quasiperiodic orbit and an irrational rotation number. This correspondence validates the H-rank as a reliable indicator of the underlying dynamical regime.

The chaotic sequences used as encryption keys in this work are the hierarchical components $\mu^{(t)}_{1,x}$, $\mu^{(t)}_{2,x}$, and $\mu^{(t)}_{3,x}$ of the Caputo fractional matrix standard map. Each sequence consists of 1000 iterates; to avoid transient effects inherent to the fractional memory kernel, the first 200 elements are discarded and the subsequent $N = 800$ elements are retained as the operative key.

The test signal is a discrete sinusoid with additive noise:

$$s(t) = \sin(2\pi f t) + \eta(t), \qquad f = 5, \tag{83}$$

sampled at $N = 800$ points, where $\eta(t)$ denotes zero-mean random noise. Three decryption experiments are performed, assuming the correct key is $\mu^{(t)}_{1,x}$: decryption with the correct key $\mu^{(t)}_{1,x}$—the signal is recovered exactly; decryption with the incorrect key $\mu^{(t)}_{2,x}$—the signal remains distorted; and decryption with the incorrect key $\mu^{(t)}_{3,x}$—the signal remains distorted.

The results are shown in Figure 8. Panel (A) displays the original signal, which exhibits clear periodicity and structure. Panel (B) shows the encrypted signal S': the permutation effectively destroys all visible structure, and the signal becomes visually indistinguishable

from random noise, confirming that inter-sample correlation has been eliminated. Panel (C) demonstrates exact recovery when the correct key is applied, restoring both the waveform and statistical properties of the original signal. Panels (D) and (E) show the results with incorrect keys $\mu_{2,x}^{(t)}$ and $\mu_{3,x}^{(t)}$, respectively: in both cases, the permutation does not match the one used for encryption, and the recovered signal remains disordered.

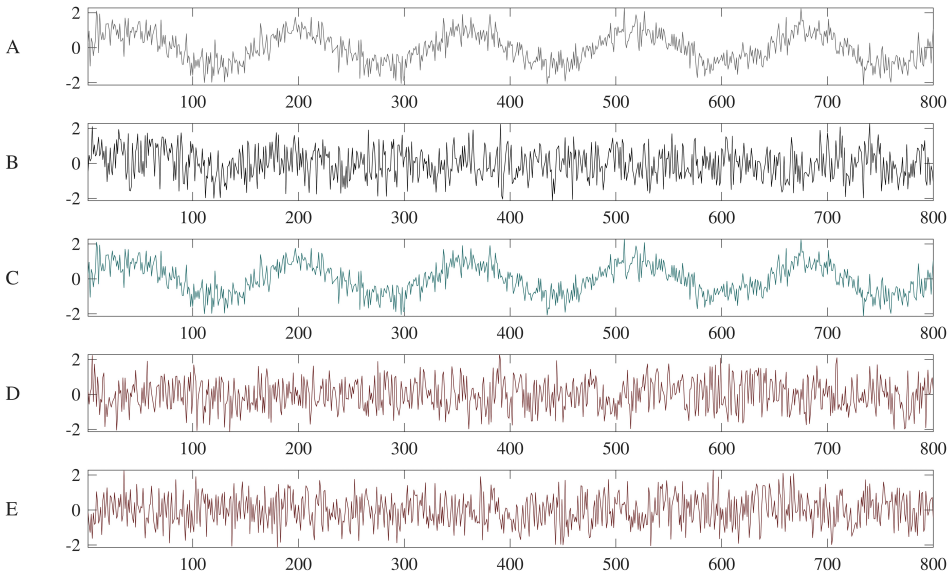

Figure 8. Signal encryption and decryption results using chaotically generated permutations derived from the hierarchical sequences $\mu_{1,x}^{(t)}$, $\mu_{2,x}^{(t)}$, and $\mu_{3,x}^{(t)}$ of the fractional matrix standard map ($\alpha = 1.001$). The hierarchical auxiliary parameters serve as encryption keys: each sequence generates a distinct permutation of the signal samples, and correct decryption requires knowledge of the exact key used for encryption. The sensitivity of the method to the choice of key is a direct consequence of the hierarchical Arnold tongue structure, where different layers produce genuinely different dynamical complexity. From top to bottom: (**A**) the original signal S, composed of a sinusoidal component and additive noise; (**B**) the encrypted signal S', obtained by applying the permutation π_1 generated from $\mu_{1,x}^{(t)}$ — all visible structure is destroyed; (**C**) decryption with the correct key $\mu_{1,x}^{(t)}$: the signal is recovered exactly; (**D**) decryption with the incorrect key $\mu_{2,x}^{(t)}$: the signal remains distorted and does not match the original; (**E**) decryption with the incorrect key $\mu_{3,x}^{(t)}$: analogous failure, confirming the key sensitivity of the method.

These results highlight two important properties of the proposed scheme. First, the three hierarchical sequences generate distinct permutations, even though they originate from the same dynamical system, as a direct consequence of the nonlinear coupling between hierarchical levels. Second, the method exhibits strong key sensitivity: an incorrect key, even one drawn from the same system, fails to recover the signal. Together, these properties suggest that the hierarchical index j can serve as an additional structural parameter in encryption design, providing independent cryptographic keys from a single trajectory of the fractional matrix map.

6. Concluding Remarks

In this work, we investigated the fractional standard map generated by nilpotent matrices of order n and demonstrated that the interplay between fractional memory and nilpotent algebra leads to the emergence of hierarchical Arnold tongues associated with divergent dynamics. The analysis was based on the algebraic structure of idempotent and nilpotent matrices and on the formulation of the corresponding fractional matrix maps.

Some important properties of the numerical scheme used in this work should be noted. The G-coefficient computational scheme retains the full fractional memory back to the

initial conditions at every time step, without any truncation or approximation. The scheme is efficient enough to handle thousands of iterations without resorting to supercomputing resources. The computations are exact up to machine epsilon, and no convergence analysis in the classical numerical sense is required. It is also important to emphasize that the blow-up behavior observed in the simulations is not a numerical artifact. It is a genuine mathematical phenomenon produced by the nilpotent algebraic structure of the system, and the algorithm itself remains stable and fully reproducible across different parameter values, fractional derivative magnitudes, and initial conditions.

It was shown that, for idempotent matrices, the fractional standard map preserves the same level of dynamical complexity as its scalar counterpart. In contrast, when nilpotent matrices are considered, the coefficients of the map become coupled through higher-order terms. This coupling produces substantially richer dynamical behavior and gives rise to hierarchies of diverging Arnold tongues that are not present in the non-fractional standard map.

To facilitate numerical investigations, an efficient computational scheme for the auxiliary parameters $\mu_{j,x}^{(t)}$ was derived, replacing falling factorial expressions by iteratively computed coefficients. The numerical implementation was calibrated using the H-rank algorithm, which provides a concise measure of the algebraic complexity of sequences generated by dynamical systems. Computational simulations revealed well-defined hierarchical structures of Arnold tongues of divergence and distinct divergence rates for the parameters $\mu_{j,x}^{(t)}$.

An important feature of these hierarchical structures is that a given point in the parameter plane may belong to regions of different colors in different hierarchical layers. Consequently, the hierarchical level associated with a particular $\mu_{j,x}^{(t)}$ becomes an essential parameter determining the algebraic complexity of the transient dynamics. In applications where transient dynamical processes are used to encode information, such hierarchical layering may provide an additional degree of freedom for information encoding. Exploring the potential of these hierarchical structures for information encoding and related security applications constitutes a natural direction for future research.

Beyond image encryption, the hierarchical layering of Arnold tongue structures suggests broader potential in secure communications. The sensitivity of the hierarchical level to the choice of system parameters and initial conditions could be exploited to design multi-layer communication protocols, where different hierarchical layers serve as independent encryption channels with distinct algebraic complexity. Such protocols would inherit the robustness and key sensitivity demonstrated in the encryption results of this work.

The hierarchical Arnold tongue structures may also find applications in the study of biological rhythms. Arnold tongues are well established in the analysis of synchronization phenomena in cardiac dynamics, neural oscillations, and circadian rhythms. The fractional memory component introduced in the present framework provides a natural mechanism for modeling the long-memory effects observed in biological systems, and the hierarchical structure of divergence may offer new tools for characterizing the complexity of transient synchronization processes in such systems.

The standard map has well-established connections to particle transport and nonlinear resonance phenomena in plasma physics and magnetic confinement fusion. The fractional nilpotent matrix framework developed in this work, with its characteristic blow-up effects and hierarchical dynamical structures, may offer new tools for studying explosive instabilities and anomalous transport phenomena in such systems. These connections open up new perspectives that warrant further exploration.

Author Contributions: Conceptualization, R.S. and M.R.; data curation, U.O.; formal analysis, R.S.; funding acquisition, M.R.; investigation, R.S., U.O. and M.R.; methodology, R.S., U.O. and M.R.; project administration, M.R.; software, U.O.; supervision, R.S. and M.R.; validation, R.S. and U.O.; visualization, U.O.; writing—original draft, R.S., U.O. and M.R.; writing—review & editing, R.S., U.O. and M.R. All authors have read and agreed to the published version of the manuscript.

Funding: This research is funded by the Research Council of Lithuania (LMTLT), Project No. S-MIP-25-52 (Finite-time divergence in differential equations of nilpotent matrices—theory and applications (DENM)).

Data Availability Statement: The original contributions presented in this study are included in the article. Further inquiries can be directed to the corresponding author.

Conflicts of Interest: The authors declare no conflicts of interest.

References

1. Arnold, V.I. Small denominators and problems of stability of motion in classical and celestial mechanics. *Russ. Math. Surv.* **1963**, *18*, 85–191. [CrossRef]
2. Ecke, R.E.; Farmer, J.D.; Umberger, D.K. Scaling of the Arnold tongues. *Nonlinearity* **1989**, *2*, 175–196. [CrossRef]
3. Rajni; Ghosh, B. Arnold tongues, shrimp structures, multistability, and ecological paradoxes in a discrete-time predator–prey system. *Chaos Interdiscip. Nonlinear Sci.* **2024**, *34*, 123103. [CrossRef] [PubMed]
4. McGuinness, M.; Hong, Y.; Galletly, D.; Larsen, P. Arnold tongues in human cardiorespiratory systems. *Chaos Interdiscip. J. Nonlinear Sci.* **2004**, *14*, 1–6. [CrossRef]
5. Levi, M.; Zhou, J. Arnold tongues in area-preserving maps. *Arch. Ration. Mech. Anal.* **2023**, *247*, 32. [CrossRef]
6. Goncharuk, N.; Yampolsky, M. Renormalization of circle maps and smoothness of Arnold tongues. *Ergod. Theory Dyn. Syst.* **2025**, *45*, 2845–2889. [CrossRef]
7. Prants, F.G.; Rech, P.C. Organization of periodic structures in a damped-forced oscillator. *Eur. Phys. J. B* **2014**, *87*, 196. [CrossRef]
8. Golden, A.; Sgro, A.E.; Mehta, P. Arnold tongues in oscillator systems with nonuniform spatial driving. *Phys. Rev. E* **2021**, *103*, 042211. [CrossRef]
9. Alraddadi, I. The asymmetric periodically forced Van Der Pol oscillator. *Eur. J. Pure Appl. Math.* **2025**, *18*, 5787. [CrossRef]
10. Qian, M.; Wang, J.Z.; Zhang, X.J. Resonant regions of Josephson junction equation in case of large damping. *Phys. Lett. A* **2008**, *372*, 3640–3644. [CrossRef]
11. Ilyashenko, Y.S.; Ryzhov, D.A.; Filimonov, D.A. Phase-lock effect for equations modeling resistively shunted Josephson junctions and for their perturbations. *Funct. Anal. Its Appl.* **2011**, *45*, 192–203. [CrossRef]
12. Benz, S.P.; Burroughs, C.J. Coherent emission from two-dimensional Josephson junction arrays. *Appl. Phys. Lett.* **1990**, *58*, 2162–2164. [CrossRef]
13. Blackburn, J.A.; Smith, H.J.T.; Gronbech-Jensen, N. Chaos and thermal noise in a Josephson junction coupled to a resonant tank. *Phys. Rev. B* **1996**, *53*, 14546–14551. [CrossRef] [PubMed]
14. de Souza, S.L.; Batista, A.M.; Caldas, I.L. Arnold tongues replace period-doubling cascades in a memristor circuit. *Chaos Interdiscip. J. Nonlinear Sci.* **2025**, *35*. [CrossRef] [PubMed]
15. Azzouz, A.; Duhr, R.; Hasler, M. Transition to chaos in a simple nonlinear circuit driven by a sinusoidal voltage source. *IEEE Trans. Circuits Syst.* **1983**, *30*, 913–914. [CrossRef]
16. Chua, L.O.; Desoer, C.A.; Kuh, E.S. Quasiperiodicity and chaos in a driven nonlinear oscillator circuit. *IEEE Trans. Circuits Syst.* **1986**, *33*, 974–980. [CrossRef]
17. Wu, X.; Peng, J.; Yuan, B.; Boscolo, S.; Finot, C.; Zeng, H. Unveiling the complexity of Arnold's tongues in a breathing-soliton laser. *Sci. Adv.* **2025**, *11*, eads3660. [CrossRef]
18. Wieczorek, S.; Krauskopf, B.; Lenstra, D. Multipulse excitability in a semiconductor laser with optical injection. *Phys. Rev. Lett.* **2002**, *88*, 063901. [CrossRef]
19. Annovazzi-Lodi, V.; Donati, S.; Manna, M. Chaos and locking in a semiconductor laser due to external injection. *IEEE J. Quantum Electron.* **1994**, *30*, 1537–1541. [CrossRef]
20. Felicio, C.C.; Rech, P.C. Arnold tongues and the Devil's Staircase in a discrete-time Hindmarsh–Rose neuron model. *Phys. Lett. A* **2015**, *379*, 2845–2847. [CrossRef]
21. Sanchez, P.G.L.; Mochulska, V.; Mauffette Denis, C.; Mönke, G.; Tomita, T.; Tsuchida-Straeten, N.; Petersen, Y.; Sonnen, K.; François, P.; Aulehla, A. Arnold tongue entrainment reveals dynamical principles of the embryonic segmentation clock. *eLife* **2022**, *11*, e79575. [CrossRef]

22. Glass, L.; Mackey, M.C. Pathological conditions resulting from instabilities in physiological control systems. *Ann. N. Y. Acad. Sci.* **1979**, *316*, 214–235. [CrossRef] [PubMed]
23. Guevara, M.R.; Glass, L.; Shrier, A. Phase locking, period-doubling bifurcations, and irregular dynamics in periodically stimulated cardiac cells. *Science* **1981**, *214*, 1350–1353. [CrossRef] [PubMed]
24. Ruhunusiri, W.S.; Goree, J. Synchronization mechanism and Arnold tongues for dust density waves. *Phys. Rev. E—Stat. Nonlinear Soft Matter Phys.* **2012**, *85*, 046401. [CrossRef] [PubMed]
25. Pikovsky, A.; Rosenblum, M.; Kurths, J. *Synchronization: A Universal Concept in Nonlinear Sciences*; Cambridge University Press: Cambridge, UK , 2001.
26. Boccaletti, S.; Kurths, J.; Osipov, G.; Valladares, D.; Zhou, C. The synchronization of chaotic systems. *Phys. Rep.* **2002**, *366*, 1–101. [CrossRef]
27. Planat, M. Nonlinear structure of phase motion from the study of differential equations near resonant tori. In *Proceedings of the Nonlinear Coherent Structures in Physics and Biology: Proceedings of the 7th Interdisciplinary Workshop Held at Dijon, France, 4–6 June 1991*; Springer: Berlin/Heidelberg, Germany, 2005; pp. 292–301. [CrossRef]
28. Ojeda Collado, H.P.; Usaj, G.; Balseiro, C.A.; Zanette, D.H.; Lorenzana, J. Emergent parametric resonances and time-crystal phases in driven Bardeen-Cooper-Schrieffer systems. *Phys. Rev. Res.* **2021**, *3*, L042023. [CrossRef]
29. Zaks, M.A.; Pikovsky, A. Frequency locking near the gluing bifurcation: Spin-torque oscillator under periodic modulation of current. *Phys. D Nonlinear Phenom.* **2016**, *335*, 33–44. [CrossRef]
30. Coombes, S.; Bressloff, P.C. Mode locking and Arnold tongues in integrate-and-fire neural oscillators. *Phys. Rev. E* **1999**, *60*, 2086. [CrossRef]
31. Jang, J.K.; Ji, X.; Joshi, C.; Okawachi, Y.; Lipson, M.; Gaeta, A.L. Observation of Arnold tongues in coupled soliton Kerr frequency combs. *Phys. Rev. Lett.* **2019**, *123*, 153901. [CrossRef]
32. Skryabin, D.; Fan, Z.; Villois, A.; Puzyrev, D. Threshold of complexity and Arnold tongues in Kerr-ring microresonators. *Phys. Rev. A* **2021**, *103*, L011502. [CrossRef]
33. Pareyon, G. Tuning systems nested within the Arnold tongues: Musicological and structural interpretations. In *The Musical-Mathematical Mind: Patterns and Transformations*; Springer: Berlin/Heidelberg, Germany, 2017; pp. 221–230. [CrossRef]
34. Borovkova, E.I.; Chernets, E.P.; Ishbulatov, Y.M.; Skazkina, V.V.; Gridnev, V.I.; Mironov, S.A.; Karavaev, A.S. Experimental observation of Arnold tongues in the analysis of the signal from contour of the autonomous regulation of heart rate and respiration. In *Proceedings of the 2019 3rd School on Dynamics of Complex Networks and their Application in Intellectual Robotics (DCNAIR)*; IEEE: Piscataway, NJ, USA, 2019; pp. 32–35. [CrossRef]
35. Fredrickson-Hemsing, L.; Ji, S.; Bruinsma, R.; Bozovic, D. Mode-locking dynamics of hair cells of the inner ear. *Phys. Rev. E—Stat. Nonlinear Soft Matter Phys.* **2012**, *86*, 021915. [CrossRef]
36. Heltberg, M.L.; Krishna, S.; Kadanoff, L.P.; Jensen, M.H. A tale of two rhythms: Locked clocks and chaos in biology. *Cell Syst.* **2021**, *12*, 291–303. [CrossRef]
37. Tarasov, V.E.; Edelman, M. Fractional dissipative standard map. *Chaos Interdiscip. J. Nonlinear Sci.* **2010**, *20*, 023127. [CrossRef] [PubMed]
38. Zaslavsky, G.M. *The Physics of Chaos in Hamiltonian Systems*; Imperial College Press: London, UK, 2007. [CrossRef]
39. Jánosi, D.; Károlyi, G. Macroscopic transport in mixed phase space Hamiltonian systems and the role of a distinct time-scale for the power-law decay. *Chaos Interdiscip. J. Nonlinear Sci.* **2024**, *34*, 081104. [CrossRef] [PubMed]
40. Meiss, J.D. *Differential Dynamical Systems*; SIAM: Philadelphia, PA, USA, 2007. [CrossRef]
41. Reichl, L.E. Area-Preserving Maps. In *The Transition to Chaos: Conservative Classical Systems and Quantum Manifestations*; Springer: New York, NY, USA, 2004; pp. 58–133. [CrossRef]
42. Edelman, M. Fractional maps and fractional attractors. Part II: Fractional difference caputo α-families of maps. *Discontinuity Nonlinearity Complex.* **2015**, *4*, 391–402. [CrossRef]
43. Podlubny, I. *Fractional Differential Equations*; Academic Press: Cambridge, MA, USA, 1999.
44. Kilbas, A.A.; Srivastava, H.; Trujillo, J. *Theory and Applications of Fractional Differential Equations*; Elsevier: Amsterdam, The Netherlands, 2006.
45. Edelman, M. Universal fractional map and cascade of bifurcations type attractors. *Chaos Interdiscip. J. Nonlinear Sci.* **2013**, *23*, 033127. [CrossRef]
46. Abdeljawad, T. On Riemann and Caputo fractional differences. *Comput. Math. Appl.* **2011**, *62*, 1602–1611. [CrossRef]
47. Atici, F.M.; Eloe, P.W. Initial value problems in discrete fractional calculus. *Proc. Am. Math. Soc.* **2009**, *137*, 981–989. [CrossRef]
48. Edelman, M. Fractional maps as maps with power-law memory. In *Nonlinear Dynamics and Complexity*; Springer: Berlin/Heidelberg, Germany, 2013; pp. 79–120.
49. Orinaite, U.; Telksniene, I.; Telksnys, T.; Ragulskis, M. How Does the Fractional Derivative Change the Complexity of the Caputo Standard Fractional Map. *Int. J. Bifurc. Chaos* **2024**, *34*, 2450085. [CrossRef]

50. Navickas, Z.; Smidtaite, R.; Vainoras, A.; Ragulskis, M. The logistic map of matrices. *Discret. Contin. Dyn. Syst.-B* **2011**, *16*, 927–944. [CrossRef]
51. Navickas, Z.; Ragulskis, M.; Vainoras, A.; Smidtaite, R. The explosive divergence in iterative maps of matrices. *Commun. Nonlinear Sci. Numer. Simul.* **2012**, *17*, 4430–4438. [CrossRef]
52. Smidtaite, R.; Navickas, Z.; Ragulskis, M. Clocking divergence of iterative maps of matrices. *Commun. Nonlinear Sci. Numer. Simul.* **2021**, *95*, 105589. [CrossRef]
53. Lu, G.; Smidtaite, R.; Howard, D.; Ragulskis, M. An image hiding scheme in a 2-dimensional coupled map lattice of matrices. *Chaos Solitons Fractals* **2019**, *124*, 78–85. [CrossRef]
54. Smidtaite, R.; Ragulskiene, J.; Bikulciene, L.; Ragulskis, M. Hyper Coupled Map Lattices for Hiding Multiple Images. *Complexity* **2023**, *2023*, 8831078. [CrossRef]
55. Smidtaite, R.; Lu, G.; Ragulskis, M. Image entropy for the identification of chimera states of spatiotemporal divergence in complex coupled maps of matrices. *Entropy* **2019**, *21*, 523. [CrossRef]
56. Smidtaite, R.; Ragulskis, M. Spiral waves of divergence in the Barkley model of nilpotent matrices. *Chaos Solitons Fractals* **2022**, *159*, 112158. [CrossRef]
57. Smidtaite, R.; Ragulskis, M. Finite-time divergence in Chialvo hyperneuron model of nilpotent matrices. *Chaos Solitons Fractals* **2024**, *179*, 114482. [CrossRef]
58. Tarasov, V.; Zaslavsky, G. Fractional equations of kicked systems and discrete maps. *J. Phys. A Math. Gen.* **2008**, *41*, 435101. [CrossRef]
59. Orinaitė, U.; Šmidtaitė, R.; Ragulskis, M. Arnold tongues of divergence in the Caputo fractional standard map of nilpotent matrices. *Nonlinear Anal. Model. Control.* **2025**, *30*, 1103–1120. [CrossRef]
60. Markovsky, I. *Low-Rank Approximation: Algorithms, Implementation, Applications*; Springer: Berlin/Heidelberg, Germany, 2012.
61. Tarasov, V. Discrete map with memory from fractional differential equation of arbitrary positive order. *J. Math. Phys.* **2009**, *50*, 122703. [CrossRef]
62. Edelman, M. Fractional standard map: Riemann–Liouville vs. Caputo. *Chaos* **2011**, *28*, 043120. [CrossRef]
63. Petkevičiūtė-Gerlach, D.; Šmidtaitė, R.; Ragulskis, M. Intermittent Bursting in the Fractional Difference Logistic Map of Matrices. *Int. J. Bifurc. Chaos* **2022**, *32*, 2230002. [CrossRef]
64. Aigner, M. *Combinatorial Theory*; Springer Science & Business Media: Berlin/Heidelberg, Germany, 2012; Volume 234.
65. Lu, G.; Landauskas, M.; Ragulskis, M. Control of divergence in an extended invertible logistic map. *Int. J. Bifurc. Chaos* **2018**, *28*, 1850129. [CrossRef]
66. Uzdila, E.; Telksniene, I.; Telksnys, T.; Ragulskis, M. Finite-Time Stabilization of Unstable Orbits in the Fractional Difference Logistic Map. *Fractal Fract.* **2023**, *7*, 570. [CrossRef]
67. Ragulskis, M.; Navickas, Z. The rank of a sequence as an indicator of chaos in discrete nonlinear dynamical systems. *Commun. Nonlinear Sci. Numer. Simul.* **2011**, *16*, 2894–2906. [CrossRef]
68. Arnold, V.I. *Geometrical Methods in the Theory of Ordinary Differential Equations*; Springer: Berlin/Heidelberg, Germany, 1983.
69. Chirikov, B.V. A universal instability of many-dimensional oscillator systems. *Phys. Rep.* **1979**, *52*, 263–379. [CrossRef]
70. Glass, L.; Mackey, M.C. *From Clocks to Chaos: The Rhythms of Life*; Princeton University Press: Princeton, NJ, USA, 1988.
71. Weyl, H. Über die Gleichverteilung von Zahlen mod. Eins. *Math. Ann.* **1916**, *77*, 313–352. [CrossRef]
72. Cachin, C. An information-theoretic model for steganography. In *Information Hiding*; Springer: Berlin/Heidelberg, Germany, 1998; pp. 306–318.
73. Kocarev, L. Chaos-based cryptography: A brief overview. *IEEE Circuits Syst. Mag.* **2001**, *1*, 6–21. [CrossRef]
74. Fridrich, J. Symmetric ciphers based on two-dimensional chaotic maps. *Int. J. Bifurc. Chaos* **1998**, *8*, 1259–1284. [CrossRef]
75. Baptista, M.S. Cryptography with chaos. *Phys. Lett. A* **1998**, *240*, 50–54. [CrossRef]
76. Alvarez, G.; Li, S. Some basic cryptographic requirements for chaos-based cryptosystems. *Int. J. Bifurc. Chaos* **2006**, *16*, 2129–2151. [CrossRef]